JGR Solid Earth

RESEARCH ARTICLE

†Deceased August 2021.

Key Points:
- Migration of seismic source in a set of explosion at Stromboli is estimated by moment tensor inversion and semblance analyses
- Source laterally migrates from the west to the crater just before an explosion, and moves back to the initial location during the explosion
- Small seismic signal in the 0.05–0.2 Hz frequency band is detected 10–20 s before the explosive onset

Supporting Information:
Supporting Information may be found in the online version of this article.

Correspondence to:
T. Nishimura,
takeshi.nishimura.d2@tohoku.ac.jp

Author Contributions:
Investigation: Giorgio Lacanna, Denis Legrand, Sébastien Valade, Maurizio Ripepe
Project Administration: Maurizio Ripepe
Supervision: Takeshi Nishimura, Maurizio Ripepe
Writing – review & editing: Shunsuke Sugimura, Takeshi Nishimura, Giorgio Lacanna, Denis Legrand, Sébastien Valade, Maurizio Ripepe

Seismic Source Migration During Strombolian Eruptions Inferred by Very-Near-Field Broadband Seismic Network

Shunsuke Sugimura[1,2,†] , **Takeshi Nishimura[1]** , **Giorgio Lacanna[2]** , **Denis Legrand[2,3]** , **Sébastien Valade[2,3]**, and **Maurizio Ripepe[2]**

[1]Department of Geophysics, Graduate School of Science, Tohoku University, Sendai, Japan, [2]Department of Earth Sciences, University of Florence, Florence, Italy, [3]Universidad Nacional Autónoma de México, Instituto de Geofísica, Ciudad de México, Mexico City, Mexico

Abstract We analyze seismic waves excited by small Strombolian explosions to understand the source process of volcanic explosions. We deployed five broadband seismometers at only 100–300 m away from the active craters of Stromboli volcano, Italy. Moment tensor inversion of the entire seismic signals in the 0.05–0.2 Hz band locates the source at a depth of 170 and 150–200 m west/southwest of the crater where acoustic waves are excited. Contrary, the sources of seismic waves in the 0.2–0.5 and 0.5–1.0 Hz bands are excited almost at the explosion onset and are located close to the crater. We show for the first time that explosions are preceded of about 10–20 s by a small amplitude seismic phase. Semblance analysis shows that this phase is radiated from a depth of 170 m beneath the western part of the crater area. Our analysis indicates that the source moves about 50 m toward the active crater 10–20 s before the explosion occurs at the surface. At the explosion onset, the source moves back to the same location of the small preceding phase. These lateral migrations of the seismic source are estimated by moment tensor inversion and semblance analysis. We suggest that migration reflects the bending of the shallow feeding system toward northeast. Seismic waves are thus reflecting the history pressure generated by the rising of a gas-rich pocket in the very shallow portion of a magma mush and by the following restoring force occurring after the explosion.

Plain Language Summary We analyze seismic waves repeatedly excited before, during and after small explosions at the summit crater of Stromboli volcano, Italy, to understand the magma motions in the shallow conduit and reservoir system. To improve the spatio-temporal resolution and detect slight movement of magma, we deployed broad-band seismometers very close to the active craters with a distance range of 100–300 m. As a result, we succeeded in clarifying detailed horizontal spatio-temporal change of seismic sources for about 1 min before and after each explosion. First seismic source, which is for the first time detected in seismogram as a very small amplitude phase, appears at a depth of about 170 m beneath the western part of the active craters. About 20 s later, the seismic source moves about 50 m toward the craters to generate an explosion. Just after the explosion, the seismic source moves back to the west where the initial small seismic source is located. Such detailed horizontal spatio-temporal change reflects the migration and/or the resonance of gas-rich magma batch in the very shallow reservoir.

1. Introduction

Strombolian eruption is one of the best known eruption styles that intermittently emit jets of gas and basaltic magma fragments (e.g., Rosi et al., 2013). This name comes from the activity observed at Stromboli volcano (924 m a.s.l.), Italy, which is located at the northern end of the Aeolian island arc in the Tyrrhenian Sea. There are three main craters within a 300 m long by 140 m wide terrace in the northern peak of the volcano (Neri & Lanzafame, 2009). Small explosions generally occur at a rate of ~13 events per hour from these craters (Ripepe et al., 2008).

Generation and migration of a large gas slug in the shallow magma reservoir system and bursting of the slug at the magma free surface have been used as a plausible mechanism of Strombolian eruption (Blackburn et al., 1976). Such large gas slug model is inferred from visual observation of the bubble bursting at the magma surface (e.g., Blackburn et al., 1976; Vergniolle & Brandeis, 1996). Two models have been proposed for the formation process of a large gas slug. One is the coalescence of gas bubbles in magma: free coalescence of small bubbles in a larger rising bubble (Parfitt, 2004; Wilson, 1980) and forced coalescence induced by the accumulation of gas bubble at

the roof of the magma reservoir (Jaupart & Vergniolle 1988, 1989; Ripepe et al., 2001) or in a bending conduit (James et al., 2004). Both models suppose that the gas bubbles ascend in low-viscosity magma due to buoyancy force and the volume rapidly increases due to decompression. As a result, a large slug migrates upward in a conduit, and generates an explosion, releasing the gas overpressure and ejecting magma fragments as pyroclasts in the atmosphere (e.g., Del Bello et al., 2012; Ripepe et al., 2001).

Vergniolle (1998) and James et al. (2008) numerically investigate the process of gas slug ascent in the conduit using the equations of motion of liquid magma and equations of state of gas in the slug. James et al. (2008) further include the motion of magma surrounding the gas slug during the ascent toward the surface. Gas slug ascent velocity and associated pressure changes measured in several laboratory experiments (e.g., Llewellin et al., 2012; Seyfried & Freundt, 2000; Vergniolle & Jaupart, 1990) are well matched with the model presented by James et al. (2008). Hence, the results of the numerical simulations and laboratory experiments have been used to quantitatively interpret the gas overpressure and the associated infrasound in terms of slug-driven Strombolian explosion (Del Bello et al., 2012; James et al., 2009).

This gas slug dynamics has been considered to be an origin of the source of very-long-period (VLP) seismic waves. At Stromboli volcano, seismic VLP signals are often observed from few seconds before to tens of seconds after each explosion (e.g., Gurioli et al., 2014; Harris & Ripepe, 2007; Ripepe et al., 2001). Moment tensor inversion analyses (Auger et al., 2006; Chouet et al., 2003) and polarization analyses (Giudicepietro et al., 2009; Marchetti & Ripepe, 2005; Martini et al., 2007) indicate that the source of VLP is located at about 500 m a.s.l. below, but outside of the crater rim in the Sciara del Fuoco slope. The estimated moment tensor solutions are explained by the opening/closing of a crack embedded in the volcanic medium (Chouet et al., 2003). Tilt motions recorded at Stromboli volcano revealed inflation-deflation cycles of ground deformation located close to the summit area (Genco & Ripepe, 2010; Ripepe, Delle Donne, et al., 2021). These inflation-deflation are repeatedly observed every a few to tens of minutes. Each explosion is preceded by a slow inflation lasting for about 200 s and the inflation rate increases about 10 times in the last 10–20 s that may indicate a drastic acceleration of the gas dynamics before the explosion (Genco & Ripepe, 2010; Ripepe, Delle Donne, et al., 2021). Ground tilt then shows a sharp deflation for ∼<30 s during and after the explosions.

Laboratory experiment on the acoustic signal associated with the growth, flow and burst of gas bubbles moving in a cylindrical reservoir with a narrow pipe (Ripepe et al., 2001) shows that a low-frequency signal is observed as soon as a gas slug starts rising in the pipe and that a high-frequency signal is excited when the gas slug breaks at the water surface in the pipe. This is similar to what we observe during explosive eruptions at Stromboli. To quantitatively compare the experimental results with the observation, the slug ascent velocity is inferred from the geophysical data. Considering the depth of the VLP source as the centroid of the reservoir, the slug ascent velocity is estimated to be 10–70 m/s (Gurioli et al., 2014; Harris & Ripepe, 2007) from the time delay between VLP and explosive onset visible on the thermal camera. Similarly, at Aso volcano, Japan, the slug ascent velocity is estimated to be 1–160 m/s for Strombolian eruptions (Ishii et al., 2019). However, these observed velocities are much faster than the theoretically predicted velocity of 1.5 and 3.4 m/s for the conduit radius of 1 and 5 m (Batchelor, 1967).

Kawaguchi and Nishimura (2015) investigated the spatio-temporal changes of volcanic deformation due to gas slug ascent in an open conduit (James et al., 2008). The result shows that the spatio-temporal characteristics and amplitudes of tilt motion observed at Stromboli (Genco & Ripepe, 2010) cannot be explained by the gas slug ascent in a conduit. These discrepancies suggest the necessity to rethink of the gas slug ascent model in favor of other mechanisms of Strombolian eruptions. More recently, a new model based on the gas flow through a shallow (<300 m) crystal mush (Barth et al., 2019) has been used to explain VLPs at Stromboli as the final stage of a ∼200 s long magma pressurization/depressurization cycle (Ripepe, Delle Donne, et al., 2021).

The objective of this study is to clarify the magma/gas dynamics associated with the origin of the seismic VLP signal at Stromboli. We deploy five seismic stations close to the craters to estimate the seismic sources with the as high resolution as possible. The stations were located at a distance of 100–300 m from the active craters, although steep topographic shape of the volcano, especially the Sciara del Fuoco, made it difficult. We apply two source location methods to clarify spatio-temporal changes of the seismic source locations before, during and after the explosive eruption. We first apply a moment tensor inversion method to the full-waveform and determine the seismic source locations (centroids). We then locate seismic sources with elapsed time based on particle motion

analyses. Finally, we compare these seismological results with a conduit model presented in previous studies and discuss the source process.

2. Temporary Geophysical Observation at the End of September 2016

The volcanic activity at Stromboli volcano have been continuously monitored by an integrated geophysical network of the University of Florence. The permanent seismic network (Figure 1) consists of four broadband seismic stations (PZZ, ROC, SCI, and STR) equipped with broadband seismometers (Güralp CMG-40T). A permanent five-element infrasonic array (EAR) allows to determine the location of the active crater. This array has an L-shape geometry with an internal spacing of ~100 m to record coherent infrasonic waves in the 1–10 Hz frequency band (Ripepe et al., 2007). Acoustic data are recorded by a 16 bits acquisition system with a sampling frequency of 54.2 Hz. These seismic and acoustic data are radio-transmitted to the monitoring center of the Department of the Civil Protection (COA) on the island, and these data are collected, processed, and published in real time on a Web site (Valade et al., 2016).

At the end of September 2016, a temporary seismic and acoustic network of five broadband stations (ST1, ST2, ST3, ST4, and ST5) was installed (Figure 1a). These stations were equipped with Güralp CMG-40T broadband seismometers and the data were recorded by 24 bits Güralp CMG24 digitizers with a sampling rate of 100 Hz. The seismometers were deployed at distances of only 100–300 m from the crater and with the aim to have the better azimuthal coverage. The acoustic signals were also recorded by infrasound microphones at the temporary stations (Lacanna & Ripepe, 2020). These seismo-acoustic stations were installed on 23 September and all the temporary stations except ST4 were withdrawn on 2 October.

3. Data Characteristics

We analyze seismic data recorded at the eight stations located within 1 km from Central (C) crater (Figure 1b). We analyze the data relative to about 17 h (from 07:05:00 to 23:59:59 UTC on 26 September 2016) which have high signal-to-noise ratio and no data gap at none of the recording stations. We select 43 seismic events associated with explosions that at ST1 show amplitudes of acoustic waves above 10 Pa. Analysis of the infrasonic array indicates that the acoustic signals are all associated with explosions occurring at the northeast (NE) crater (Figure 2).
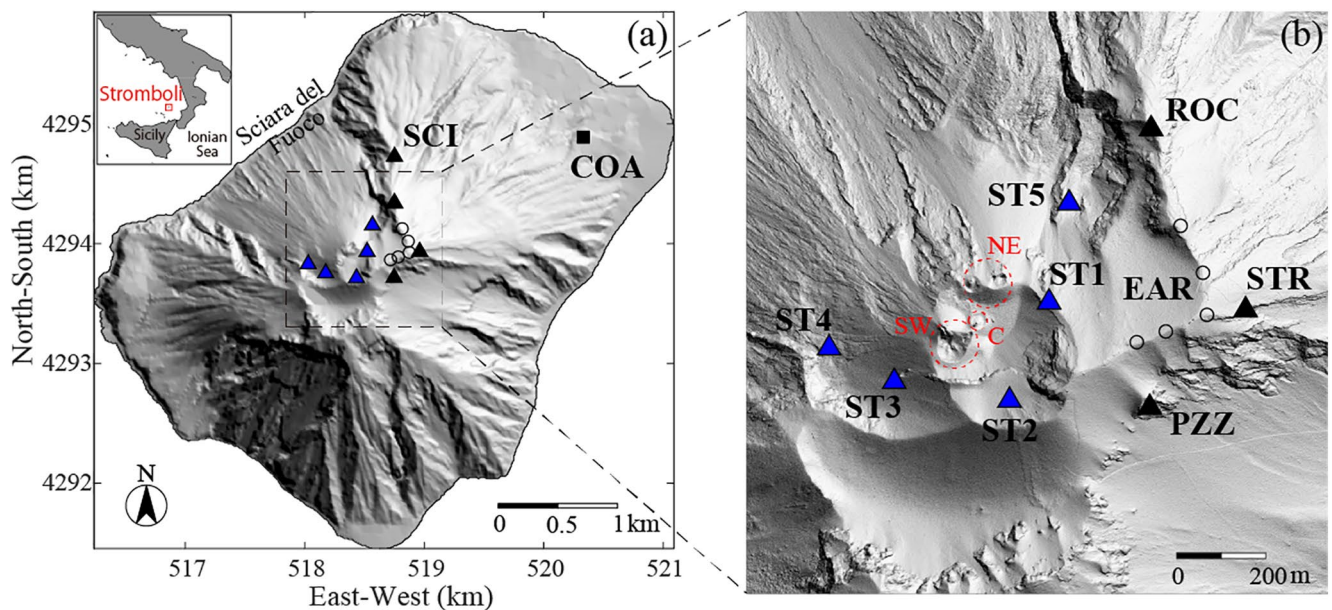
Figure 1. (a) Shaded relief map and location of the geophysical sensors at Stromboli volcano. The blue triangles represent the temporary seismic stations. The black triangles represent the permanent seismic stations of the University of Florence (PZZ, SCI, STR and ROC). The L-shape infrasonic array (EAR) is represented by the black circles. The signals are digitally transmitted and processed in real time at the operations center (COA) of Department of Civil Defense (black square). (b) Enlarged view around three active craters. The NE, C and SW craters are shown by the dashed red circles.
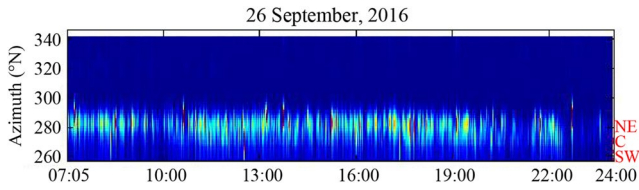
Figure 2. Back-azimuth of infrasound recorded by the L-shape infrasonic array (EAR) on 26 September 2016. The color scale indicates the signal coherence, where warmer color represents higher coherence of the infrasonic waves in the array. The bin size used is 0.21 s in time and 0.43°–1.19° in azimuth ranges. During the 17-h observation period, the Strombolian activity was mainly located at NE crater.
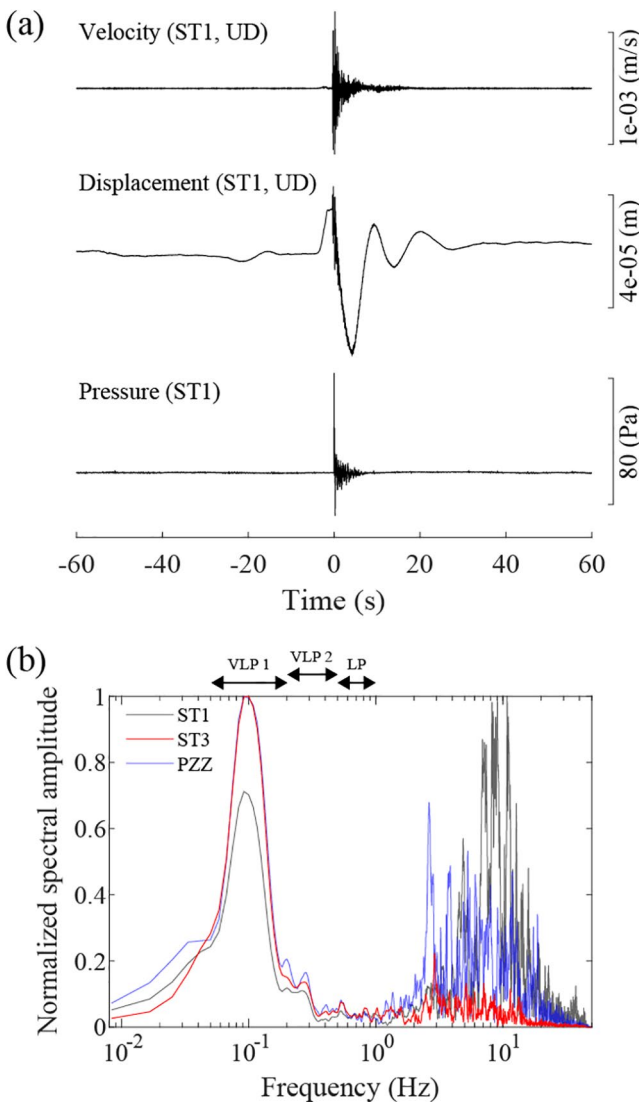
Figure 3. (a) Example of velocity and displacement seismogram, and acoustic signal at ST1 recorded during an explosion at the NE crater (on September 26, 2016, at 09:55:46 GMT). (b) Fourier spectra of velocity seismograms at ST1 (black), ST3 (red) and PZZ (blue). Fourier spectra are normalized. The frequency bands of VLP1 (0.05–0.2 Hz), VLP2 (0.2–0.5 Hz) and LP (0.5–1.0 Hz) are represented by the arrows on the top of panel.

An example of seismic and acoustic signals associated with an explosion recorded at ST1 is shown in Figure 3. This station records acoustic signals with the largest amplitudes among all the network. Ground displacement derived from the ground velocity seismogram shows that upward (compression) VLP signal is followed by large downward (rarefaction) amplitude of VLP seismic signal that starts at the onsets of high frequency seismic and acoustic signals (see Ripepe, Delle Donne, et al., 2021 for details). Spectral analysis of the ground velocity seismogram indicates that there are dominant spectral peaks around 0.1 and 10 Hz (Figure 3b). However, peaks are not the same at all the stations. For example, large spectral amplitude around 10 Hz at ST1 may be attributed to site effects, because at other stations (ST3 and PZZ) dominant frequencies are instead at around 0.1 and 2–5 Hz, which are typical frequency ranges at the permanent stations of Stromboli volcano (Ripepe, 1996).

Seismic data are analyzed in three frequency bands: (1) 0.05–0.2 Hz (periods of 5–20 s, VLP1), (2) 0.2–0.5 Hz (2–5 s, VLP2), and (3) 0.5–1.0 Hz (1–2 s, LP). The VLP1 band is the lower frequency part of the VLP (0.05–0.5 Hz, 2–20 s; e.g., Chouet et al., 2003), and represents the dominant frequency content in the seismograms. VLP2 band is the higher frequency part of the VLP, in which small spectral peaks are found at about 0.2 Hz (5 s) and 0.27 Hz (3.7 s) (Figure 3b). The LP frequency band represents the component between the two typical dominant frequencies: around 0.1 and 2–5 Hz (Ripepe, 1996). Figure 4 shows causal-filtered (fourth order) seismograms in the three VLP1, VLP2 and LP bands. Initial motions with large amplitudes are almost simultaneously detected for the three different frequency bands. Since the seismic network was deployed within a distance of about 1 km from the craters, these phases mainly consist of near-field term of the seismic waves.

Besides, the analysis of the VLP1 band shows that 21 events (out of the 43 events) have a small-amplitude positive signal that precedes by 10–20 s the onset of the explosion (Figure 5a). The amplitude of this phase is only about 2–3 times larger than the ambient noise (Figure 5b). This preceding phase is more evident when the VLP1 phase is large (Figure 5c), and it is probably masked by the ambient noise or permanent tremor when the amplitude of VLP1 band is small. This preceding phase is visible only in the VLP1 frequency bands and seems to coincide with the drastic acceleration of the ground inflation detected by tilt sensors (see Figure 6 in Ripepe, Delle Donne, et al., 2021, for details). Therefore, the preceding phase is an important signal that may represent the motions of magma and/or gas in the magma reservoir or conduits in the last tens of seconds before the explosive onset.

4. Source Location Analyses

4.1. Moment Tensor Inversion for Different Frequency Band

We first determine source locations (centroids) and mechanisms by using the entire seismic signal in the three VLP1, VLP2, and LP bands. We apply the moment tensor inversion method of Maeda et al. (2011). This method is developed to deal with horizontal seismograms strongly contaminated by tilt motions. The equations used for the method and the computation system are described in detail in Appendix A.

We compute the Green's functions by using the open-source software package of Seismic Wave Propagation Code (OpenSWPC, Maeda et al., 2017). This numerical simulation code of seismic wave propagation is based on the staggered-grid finite difference method with the fourth-order accuracy in space
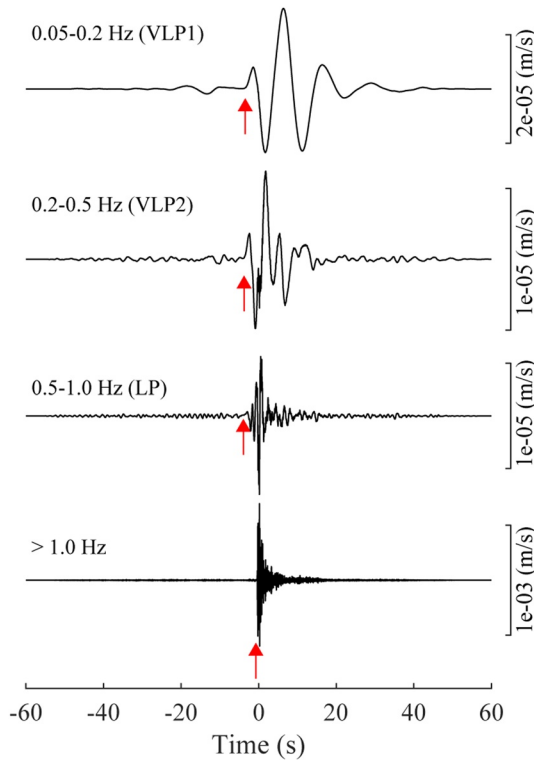
Figure 4. Causal band-pass filtered seismograms at ST1 (UD component) in the different frequency bands: 0.05–0.2, 0.2–0.5, 0.5–1.0, and above 1 Hz. This event is the same as shown in Figure 3. The arrival time of each signal is shown by a red arrow.

and second-order accuracy in time (Levander, 1988). The topography of Stromboli is obtained from a digital elevation map with a resolution of 0.5 m (Lacanna & Ripepe, 2020) and is decimated to 10 m for this computation. We assume P-wave velocity V_p of 3.5 km/s, S-wave velocity V_s of 2.0 km/s, and the medium density ρ of 2650 kg/m^3 (Chouet et al., 1998, 2003). The node spacing of the point sources is set to be 50 m. Considering the topographic condition at Stromboli, the volcanic edifice is described by 637 point sources.

The optimal source location and mechanism is defined by grid searching the minimum misfit between the observed and the synthetic seismograms. The misfit is calculated as (e.g., Ohminato et al., 1998):

$$E_1 = \frac{\sum_{n=1}^{N_t} \sum_{k=1}^{N_s} \left(U_n^{\text{obs}}\left(k\Delta t\right) - U_n^{\text{syn}}\left(k\Delta t\right) \right)^2}{\sum_{n=1}^{N_t} \sum_{k=1}^{N_s} \left(U_n^{\text{obs}}\left(k\Delta t\right) \right)^2}, \tag{1}$$

where $U_n^{\text{obs}}(k\Delta t)$ and $U_n^{\text{syn}}(k\Delta t)$ are k-th time sample of the observed and synthetic seismograms, respectively, N_t is the number of signals and N_s is the number of samples in each signal. The total number of samples for estimating E_1 is fixed at 3000, which corresponds to the time interval of 30 s (from −10 to +20 s) around the onset (see Figure 3a).

The observed and the synthetic seismograms are zero-phase Butterworth band-pass filtered in the three frequency bands (VLP1, VLP2, and LP), and the inversion method is applied to the seismograms filtered in each band. Note that positive x and y directions are set to be north and east, respectively, and z direction is the vertical one with positive downward movement, which follows the coordinate system in OpenSWPC.

Results in the VLP1 band for an event occurred at 17:02 on 26 September 2016 are shown in Figure 6. The optimal location is placed around the edge of the southwest (SW) crater, 150–200 m south-west of NE crater where acoustic waves locate the source of the explosion (Figure 6a). The minimum misfit E_1 is estimated to be 10.6% around the optimal source. The shaded area in Figure 6a represent the extension within twice the minimum residual, which corresponds to the confidence interval of 68% (see details in Section 5.2). The observed seismic waves are well explained by the synthetic ones calculated from the best fit model (Figure 6b). Figures 6c and 6d show the time function and the eigenvectors of the moment tensors. The moment tensor solution indicates the vertical dipole component, M_{zz}, in the source mechanism is dominant. Even when a different P-wave velocity V_p of 2.0 km/s estimated by tomography for the shallow layer (Patanè et al., 2017) and S-wave velocity V_s of 1.16 km/s are used in the computation of the Green's functions, the source location and mechanism do not change but they remain almost the same and in the same place (Figure S1 in Supporting Informarion S1).

Figure 7 shows the result for the VLP2 (0.2–0.5 Hz) frequency band. The optimal location is calculated to be 100 m more east than that of VLP1 (Figure 7a). The minimum misfit E_1 is 14.1%, larger than that of VLP1 (Figure 7b). The shaded area in Figure 7a represents twice the minimum residual. The source mechanism solution indicates that a dipole moment tensor components is dominant (Figure 7c), although the polarity of one dipole component (M_{zz}) is opposite to the other two components (M_{xx} and M_{yy}).

In the case of the LP (0.5–1.0 Hz) frequency band (Figure 8), the best location is approximately only 100 m east of the NE crater (Figure 8a). Figure 8a shows the map distribution of E_1 around the optimal source, which has a minimum misfit E_1 of 22.6% (Figure 8b). The time function of the moment tensors (Figure 8c) indicates a dipole moment tensor components (M_{xx}, M_{yy}, and M_{zz}) with roughly the same polarity.

The estimated source locations for the 43 events in the VLP1, VLP2, and LP frequency bands are represented in Figure 9. The gray color bars indicate the numbers of the optimal source locations estimated for the 43 events. For the VLP1 band, we have that 29 out of the 43 events are located around the rim of the southwest (SW) crater (location A) (Figure 9a). These locations are distributed around 600 m a.s.l. and 150–200 m southwest of the NE
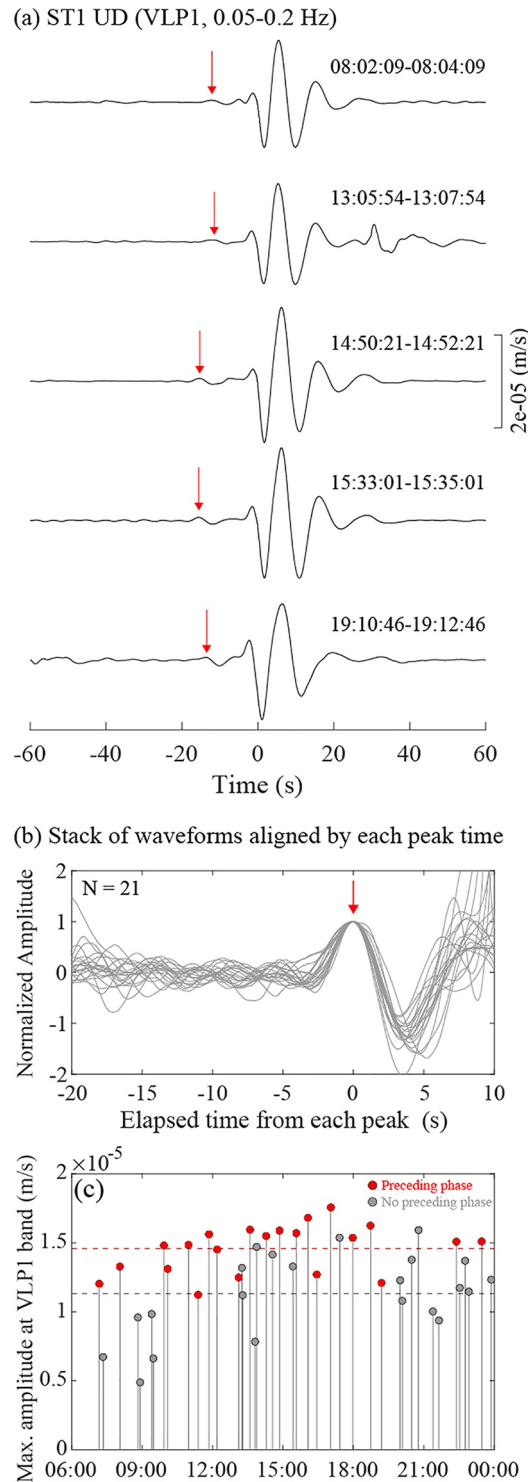
Figure 5. (a) Examples of causal-filtered seismogram in the 0.05–0.2 Hz at ST1. Small preceding phase is recognized (red arrows) before the Main phase1. (b) Preceding phases of 21 events are aligned at 20 s before the peak amplitude. Amplitudes are normalized. (c) Temporal distribution of the maximum seismic amplitudes in the VLP1 band (ST1, UD component) occurred on 26 September 2016. The red and gray dots represent the events with and without the preceding phase, respectively. The dashed lines represent the average amplitudes of the events with (red) and without (gray) the preceding phase.
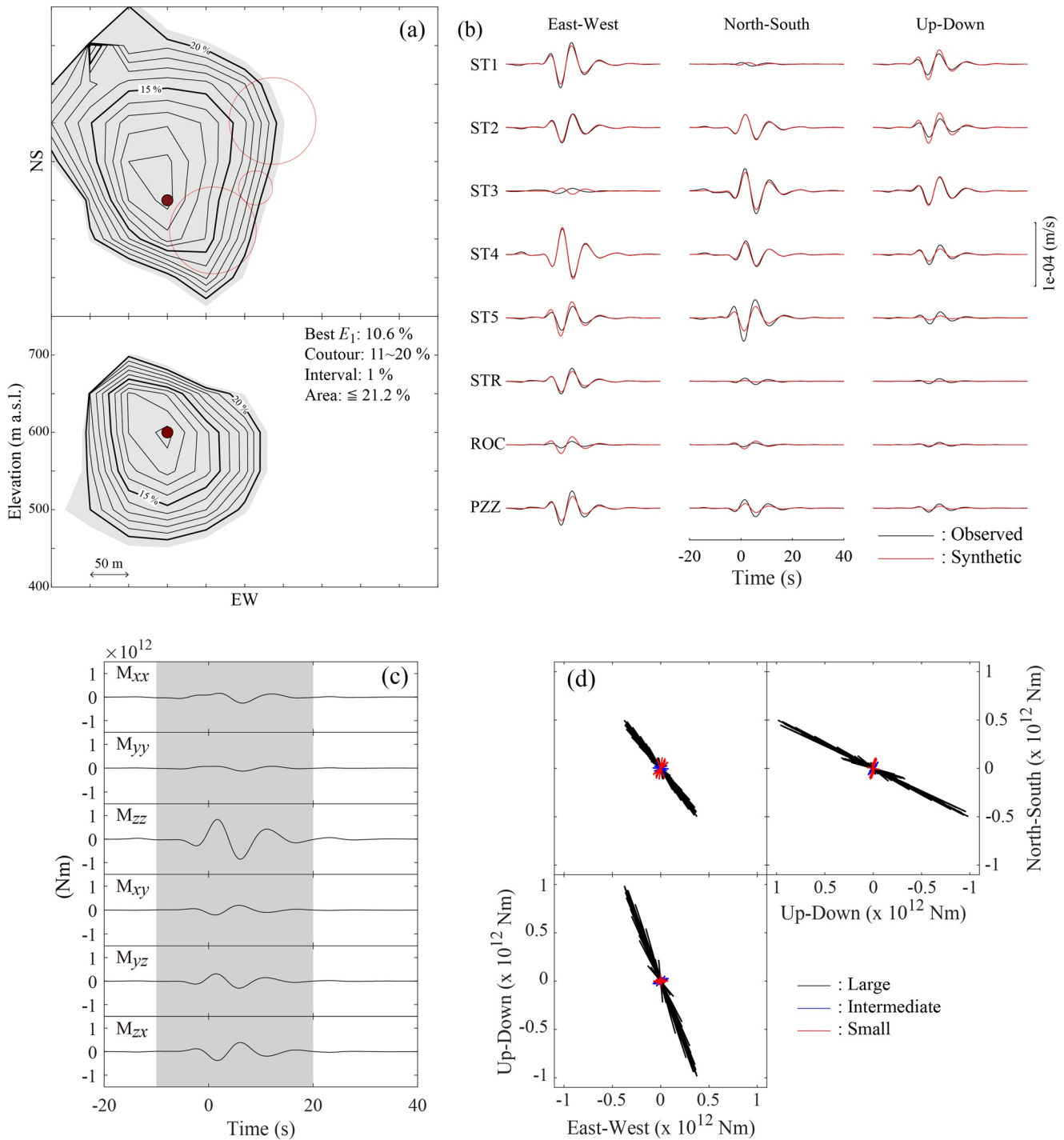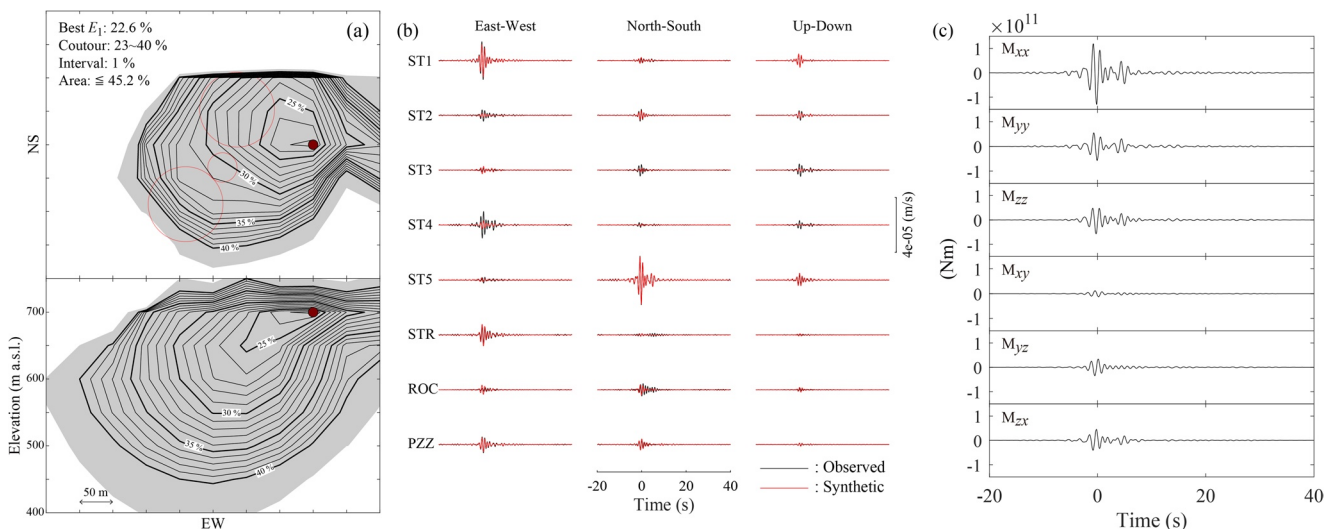
Figure 6. Solution of the moment tensor inversion analysis of the VLP1 frequency band of the signal recorded at 17:02 on September 26, 2016. (a) Contour lines of waveform residuals (E_1) around locate the source of VLP1 (red dot) with a misfit E_1 of 10.6%. The contour lines are drawn from 11% to 20% with an interval of 1%. The shaded area shows the area within twice the minimum residual, which corresponds to the confidence interval. Red large circles show the NE, C and SW craters. (b) Comparison between the observed (black) and synthetic (red) waveforms. (c) Moment tensor source time function. Note that the positive directions of x, y and z are set to be north, east, and vertical downward. (d) Eigenvectors of the moment tensor time function. The eigenvectors are determined every 0.5 s in a time window (shaded section in Figure 6c) between −10 and 20 s.
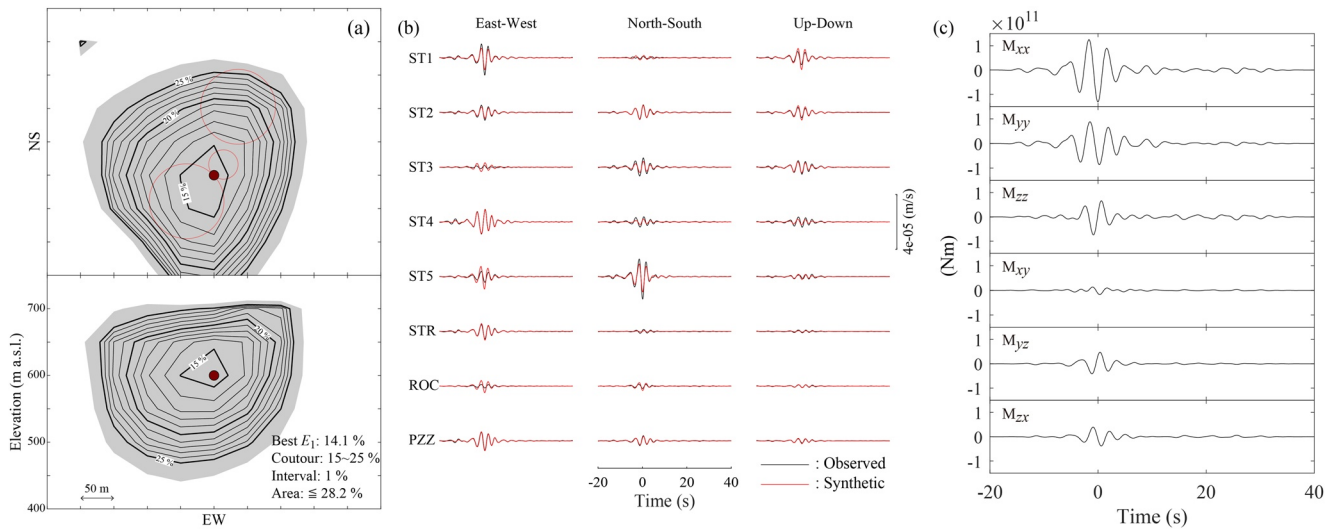
Figure 7. Solution of the moment tensor inversion analysis using the VLP2 frequency band of the signal recored at 17:02 on September 26, 2016. (a) Contour lines of waveform residuals (E_1) locate the source of the VLP2 with a misfit of 14.1%. The contour lines are drawn from 15% to 25% with an interval of 1%. The shaded area shows the area within twice the minimum residual, which corresponds to the confidence interval. Red large circles show the NE, C and SW craters. (b) Comparison of the observed (black) and synthetic (red) waveforms. (c) Moment tensor source time function.

crater. This depth is about 100 m shallower than the previous values derived by moment tensor inversion (Chouet et al., 2003) and ground deformation (Ripepe, Delle Donne, et al., 2021). Misfits E_1 are estimated to range between 9.6% and 11.1% for all the events located in A. The other 14 out of the 43 events, are located in B, C and D, 50–100 m southwest of location A. For these events, the source time functions derived by moment tensors are not the same but similar to those of location A, with a M_{zz} component dominant (Appendix B) and small misfits (10.0%–12.4%).

Source location of the VLP2 frequency band (Figure 9b) is mainly distributed just below the craters and at 50–150 m eastward from the location of the VLP1 and with a misfit (E_1) between 11.0% and 23.9%. The LP component of the seismic signal has the source, instead, mostly located at the center of the craters (Figure 9c), a little eastward than the location of VLP2 component, and with a misfit (E_1) of 15.4%–34.1%. Compared to the locations of VLP1, those of VLP2 and LP tend to be more scattered reflecting the frequency increase of the seismic

Figure 8. Same as Figure 7 for the LP band.
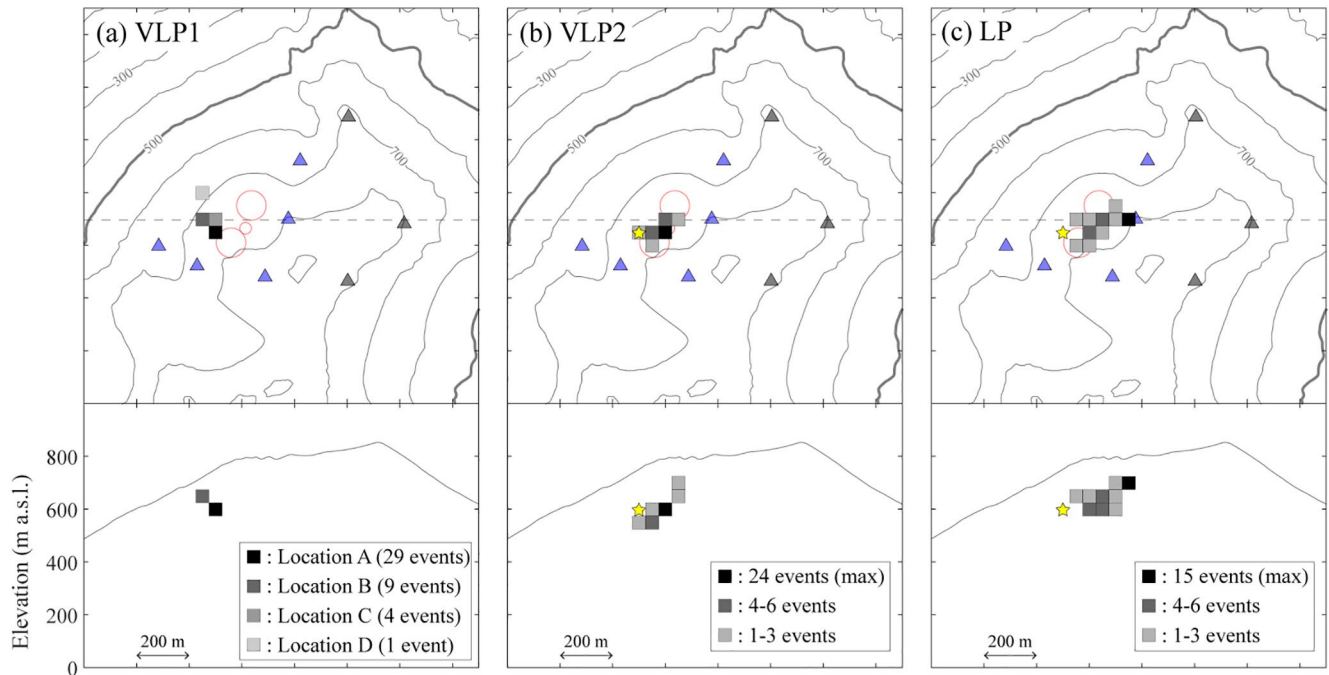
Figure 9. (a) Source distribution of the 43 seismic events determined by the moment tensor inversion in the VLP1 frequency band. Grid interval is 50 m. The number of source located in each node of the grid is indicated by gray colors. Blue and black triangles represent the seismic stations. Dashed lines indicate the position of the cross sections. Red circles represent the NE, C and SW craters. (b) Source distribution of the 43 events determined by the moment tensor inversion in the VLP2 band. Yellow star indicates the most frequent location of the VLP1 source in Figure 9a (Location A). (c) Source distribution of the 43 events determined by the moment tensor inversion in the LP band.

signal. The spatial resolution of the estimated source locations and the reliability of the source mechanisms is discussed in details in Chapter 5.

It is noted that the moment tensor inversion method determines the centroid of the source that explains the entire waveforms for about 30s. VLP1 signal begin shortly before the onset of an explosion (Figure 3a), but the larger amplitude is recorded only after the explosion occurs (Figure 4). Hence, a volumetric change at a depth of 170 m beneath the western edge of the crater area mainly occurs during and/or after the explosion (see Ripepe, Delle Donne, et al., 2021 for details). Besides, seismic waves in the VLP2 and LP frequency bands have the onset which mainly coincides with the explosion so that these waves can be associated with the triggering process of the eruption itself.

4.2. Source Locations Estimated by Semblance Analysis

We determine source location of the eruption seismic signals by particle motions and semblance analysis. Contrary to the moment tensor inversion, the semblance analysis has the merit to improve the location due to the time resolution. This enables us to examine the spatio-temporal changes before, during and after the explosion, although the assumption that the source is simply isotropic may not be realistic.

As shown in Figure 5, a preceding phase with a small amplitude is visible at all seismic stations in the VLP1 band 10–20 s before the onset of the explosion. Seismic waveform in the VLP1 band is thus divided into three parts: Preceding phase, Main phase1 and Main phase2 (Figure 10a). The time window for Preceding phase starts 30 s before the onset of the acoustic signal and lasts 20 s. Main phase1 defines the waveform just before an explosion: it starts at the end of Preceding phase and it lasts until the onset of seismic signal associated with the explosion. Main phase2 corresponds to the waveform just after the explosion onset, starts at the end of the Main phase1 and it lasts 30 s after the explosion. In conclusion, assuming the onset of the explosion as the time zero the Preceding phase ranges between −30 and −20 s, Main phase1 goes from −10 to 0 s, and Main phase2 from 0 to 30 s (Figure 10a)
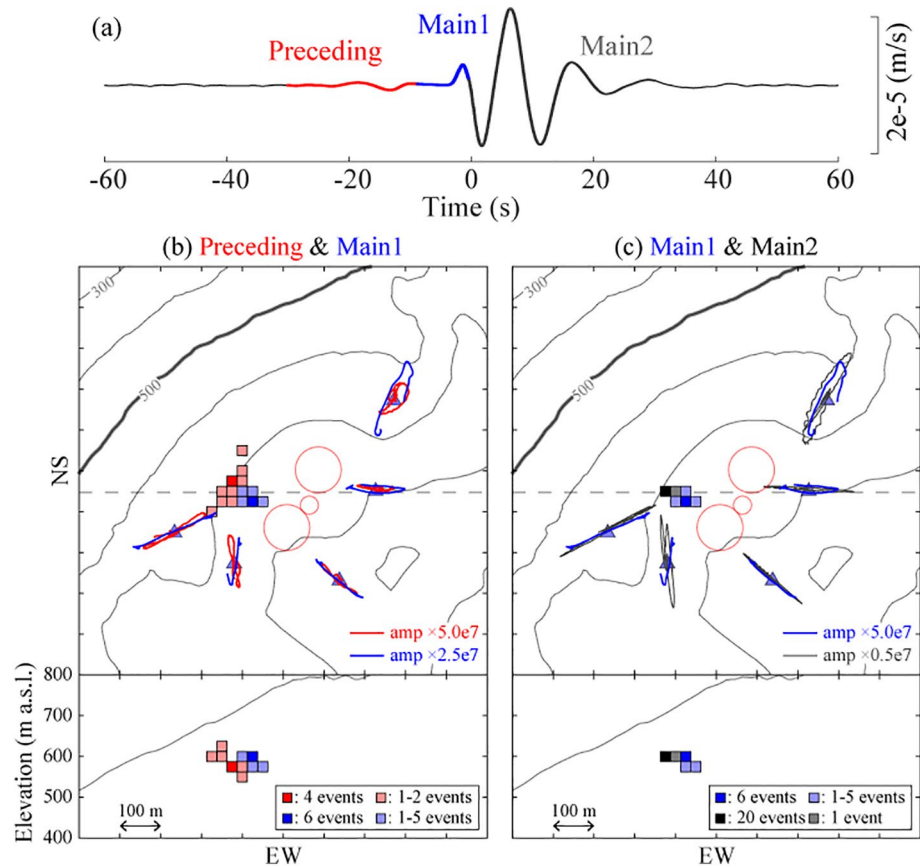
Figure 10. (a) Preceding phase, Main phase1 and Main phase2 defined in the VLP1 frequency band recorded at the ST1 station in the UD component. (b) Position of the seismic sources calculated by semblance analysis for the Preceding phase (red) and the Main phase1 (blue). The map shows a closeup around the NE, C and SW craters (red circles). Grid interval is 25 m. The number of events located at each node of the grid is indicated by different colors. Horizontal particle motions at the temporary stations (ST1-ST5) deployed in the very-near-field condition. The horizontal particle motions are multiplied by the values shown in the panel. (c) Distribution of seismic sources of Main phase1 (blue) and Main phase2 (black).

Particle motions of these three phases at the very-near-field stations (ST1-ST5) show strong rectilinearity (Figures 10b and 10c), While particle motion for the Preceding phase is pointing to the western area of the craters (Figure 10b), for the Main phase1 is directed more to the east toward the craters. In this case, particle motion coincides with the location of the VLP2 and LP frequency bands as defined by the moment tensor inversion (Figures 10b and 10c). Note that particle motion of Main phase2 points again back to the western portion of the crater area (Figure 10c). These temporal changes suggest that the source of the VLP1 migrates from west to east toward the crater before an explosion and goes back to the west during the explosion itself (Figure S2 in Supporting Informarion S1).

To better estimate this migration of the seismic source in the VLP1 frequency band, a semblance analysis following the method of Kawakatsu et al. (2000) is applied to the three different phases of the VLP1 frequency band. This method measures waveform coherency among the stations where high coherence indicates that the seismic energy is isotropically radiated from the source to the stations as compressive body waves. Semblance can be defined in order to incorporate also the information contained in the rectilinearity of the particle motions by emphasizing the radial component (R) and subtracting the other components (V, H) as follows:

$$S_3 = \frac{1}{D} \sum_{j=1}^{L} \left\{ \left(\sum_{i=1}^{N} R_{i,j(i)} \right)^2 - N \left(\sum_{i=1}^{N} V_{i,j(i)}^2 \right) - N \left(\sum_{i=1}^{N} H_{i,j(i)}^2 \right) \right\}, \qquad (2)$$

where L is the total number of samples for a target phase, N is the total number of stations, $R_{i,j(i)} \equiv R_i(t_i + j\Delta t)$ is the radial component of the seismogram at i-th station at $j(i)$-th sample from the initial time t_i which is shifted by the travel time from an assumed source to the station distance, $V_{i,j(i)}$ is the component in the direction perpendicular to $R_{i,j(i)}$ within the vertical plane which contains both source and receiver, and $H_{i,j(i)}$ is in the horizontal component perpendicular to both R and V. The scaling factor D can be taken as

$$D = N \sum_{j=1}^{L} \sum_{i=1}^{N} R_{i,j(i)}^2. \tag{3}$$

Before calculating Equation 2, each seismogram is normalized to give equal weight to each station. The root-mean-square amplitude of signal of each station is normalized as follows,

$$\text{RMS}_i^2 = \frac{1}{L} \sum_{j=1}^{L} \left(R_{i,j(i)}^2 + V_{i,j(i)}^2 + H_{i,j(i)}^2 \right) = 1. \tag{4}$$

We calculate the semblance values at each node of the grid. Grid interval is set to be 25 m, a P-wave velocity of 3.5 km/s is assumed (Chouet et al., 1998, 2003) and eight stations are considered to locate 21 events (Figures 10b and 10c). Source location of the Preceding phase is calculated to be 150–250 m west of the NE crater (Figure 10b), with a semblance (S_3) of 0.67. The Main phase1 is instead located 0–75 m eastward of the Preceding phase (Figure 10b) and has a semblance (S_3) of 0.86. The mean distance between the source locations of the two phases is 54.5 m. Source location with semblance ranging around 0.86 show that the Main phase2 (Figure 10c) is in average 42.9 m west of the location of the Main phase1. Source depths for all the three phases are stable almost at the same elevation of around 600 m a.s.l.. These results suggest that the source moves eastward toward the crater before an explosion, and then moves back westward to the initial source position during the explosion.

5. Resolution and Accuracy of the Results

Our moment tensor analysis for the three VLP1, VLP2, and LP frequency band shows a significant volumetric component at the source but with clear differences in the distributions of the M_{xx}, M_{yy} and M_{zz} components. The best-fit of the source locations (centroid) for the three VLP1, VLP2, and LP frequency range are located about 100–300 m in the east-west direction. Semblance analysis shows that the source of the VLP1 migrates in the eastward direction before and after an eruption. Such differences in source mechanism and location of the different frequency components (VLP1, VLP2, and LP) of the seismic signal recorded at Stromboli may reflect spatio and temporal changes of magma dynamics during the explosive process. Here, we carefully examine these differences by estimating the errors and performing the inversion using synthetic tests.

5.1. Moment Tensors

To verify the reliability in the observed difference of the source mechanism solutions, we calculate model resolution matrices (Menke, 1984; Stein & Wysession, 2003) to understand how well parameters can be resolved by our inversion. The model resolution matrices are calculated from the singular-value decomposition of the Green's functions used in Section 4.1. The results show that there are trade-offs between the diagonal components of the moment tensors. Resolution of the diagonal components (M_{xx}, M_{yy}, and M_{zz}) is estimated to be 0.54, 0.88, and 0.66, respectively, and their covariances range from −0.39 to −0.20 (see Appendix C). Hence, we conclude that the geometry of the source mechanism such as crack or spherical is not well constrained. This means that we are not able to discuss the differences in the source mechanisms between the different seismic VLP1, VLP2, and LP spectral component.

5.2. Source Locations Determined by Moment Tensor Inversion

To verify the reliability of our source location, we perform four different tests to estimate possible errors in our location procedure. The first analysis is based on the statistics of waveform residuals and the spatial distribution of the misfit E_1 (Equation 1). The second one is a jackknife test which allow to examine the effect of station distribution on the source locations. Third and fourth analyses consist of two synthetic tests aimed to investigate the effects of noise and network configuration on the moment tensor solutions.
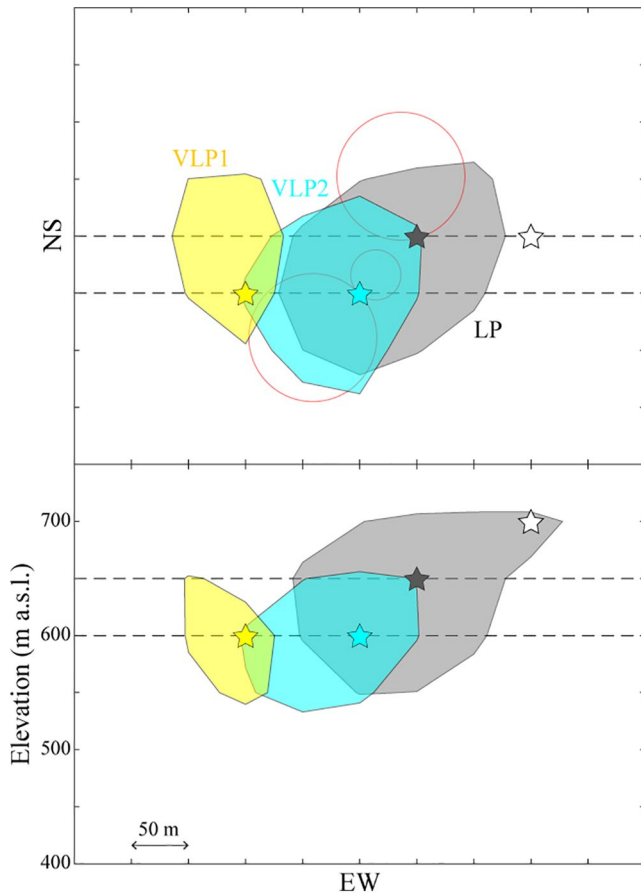
Figure 11. The best-fit of the source location calculated for the 43 seismic events in the three frequency bands: VLP1 (yellow star), VLP2 (light blue star) and LP (gray star). Their confidence level of 68% is shown by the colored area around the location. The white star shows the most frequent location of LP in Figure 9c. The dashed lines represent the position of the vertical cross sections.

We estimate errors in the location of the VLP1, VLP2, and LP sources from the confidence intervals of the spatial distributions of the misfit E_1. When the frequency distribution of the waveform residuals satisfies the normal distribution, the area within one standard deviation corresponds to the area within twice the minimum residual (e.g., Menke, 1984). The confidence interval of the VLP1 for a single event (Figure 6) corresponds to the area (21.2%) shown in Figure 6a, given that the minimum is 10.6%. As a result, the location errors determined from one standard deviation come to be approximately ±200 m in the north-south direction and ±150 m in the east-west direction, respectively. To improve the accuracy and reduce errors in the location, we consider that the seismic events at Stromboli repeat with the same waveform and thus all share the same source location and mechanisms. Therefore, we stack the probability density distributions of the misfit E_1 for all the events according to the central limit theorem (e.g., Menke, 1984). The spatial distributions of E_1 for the 43 events give the minimum and the standard deviation of the "average E_1". Dividing by the square-root of the total number of event (43), we estimate the confidence intervals for the three VLP1, VLP2, and LP bands (Figure 11). The minimum of the stacked E_1 for the VLP1 is located in A (Figure 9a), with a 68% confidence interval to be ±50 m in the east-west and vertical directions, and ±50–100 m in the north-south direction (Figure 11). In the case of the VLP2, the minimum E_1 coincides with the most frequent location (Figure 9b). While for the LP frequency range, the minimum E_1 is estimated to be 100 m east and 50 m below the most frequent location (Figure 9c), although the difference in the stacked residuals at the two locations is only 0.2%. For the VLP2 and LP frequency bands, the confidence intervals of the stacked E_1 distribution covers an area which is ±50–100 m large in each direction. As shown in Figure 11, the estimated source locations within one standard deviations for the VLP1, VLP2, and LP frequency bands do not significantly overlap to each other. Therefore, we conclude that the VLP1, VLP2, and LP source locations are distributed in the east-west directions beneath the craters and are about 100–300 m apart from each other. Further observation and analysis of more seismic events will probably improve this result and will provide more reliable solutions.

A jackknife test on the moment tensor inversions for the three frequency bands is performed using four different station geometries: (1) only the five temporary stations (ST1-ST5) deployed in the very-near-field, (2) all the stations, including the permanent seismic network, but without ST3, (3) all the stations but without ST4, and (4) all the stations without ST5. We analyze the same event shown in Figures 6–8. The result of the test shows that when the record at one station is not used, the best-fit sources are shifted between 0 and 158 m (three grid points in one direction with one grid point in another direction) from the optimal solution estimated by using all the stations (Figure S3 in Supporting Informarion S1). These differences in the location are almost the same as the confidence intervals estimated from the probability density distributions of the waveform residuals (Figure 11). When we use only the five very-near-field stations, VLP1 and VLP2 are located very far (255 and 292 m) from the optimal source. The jackknife test shows that when the number of stations and the azimuthal coverage are insufficient or when we remove the stations with the larger seismic amplitudes, source location becomes unstable.

In addition, we performed synthetic test to evaluate the effect of noise on the location. Synthetic waveforms were calculated for two different source models. The first one is an isotropic expansion/contraction source represented by a moment tensor having only diagonal components (M_{xx}, M_{yy}, and M_{zz}) with a ratio of 1:1:1. The second one is a horizontal opening/closing crack similar to the best-fit solution previously found and with a moment tensor having diagonal components of 1:1:3. In both cases, source location is set to be in location A (Figure 9a).

The Green's functions calculated for each station are then convolved with a source time function derived by the vertical component of the VLP1 frequency band recorded at ST1. We then add random noise with amplitude

different for each station, according to the signal-to-noise ratio associated with the 43 events considered in our analysis. We thus calculate 43 synthetic pseudo-VLP1 signals by randomly changing the noise. Moment tensor inversion was then applied to each pseudo-VLP1 to calculate the effect of the noise on the source location. This test shows that source location distribution for the two assumed source models (Figure S4 in Supporting Information S1) mainly coincides with the location A at least for 40 out of 43 of the pseudo-VLP1 signals calculated for the isotropic source and 38 out of 43 for the horizontal crack, respectively. In the case of the isotropic source, the misfit (E_1) of the 40 events located in A is around 0.4%–4.3%, while the other three events have misfit as large as 3.9%–11.1%. When the horizontal crack is considered, the misfit of the 38 events in A is 2.5%–10.7%, while the other 5 events range between 0.9% and 9.5%. We note that residuals of these synthetic tests are smaller than those estimated for the observed data. We suggest that this probably reflects the migration of the source position with time in the recorded VLP1 waveform which is instead assumed stable for the synthetic pseudo-VLP1 calculated for the two source models. Our synthetic tests demonstrate that we are not able to discriminate among location difference spaced out of 1 or 2 grids (50 or 100 m) using only the misfit, which remains almost in the same range of confidence (Figure 11). We do not exclude that some noise level may introduce a larger error also beyond the one or 2 grids distance. Location D estimated from real data (Figure 9a) may be explained by such noise contamination.

Finally, our second synthetic test examines how the solutions of the moment tensor inversion are affected by the network configuration. We compare our very-near-field network with a network of 18 pseudo stations located between 500 and 1000 m away from the central crater C (Figure S5 in Supporting Information S1) which reproduces the network geometry of previous experiments (e.g., Chouet et al., 2003). We generate pseudo-VLP1 by assuming three source models: (i) isotropic expansion/contraction source (ISO), (ii) opening/closing crack with N45 E striking direction, that is, parallel to the long axis of the crater terrace, and with a ratio between the principal axes of the moment tensor of 1:1:3 (Crack1), and (iii) a horizontal sill-like crack opening/closing source with a moment tensor having diagonal components of 1:1:3 (Crack2). Source location is always set to be in location A (Figure 9a). We perform moment tensor inversion by using pseudo-VLP1 calculated for the two networks. Distribution of E_1 shows that the area with the small misfits estimated for our very-near-field seismic network is between 30% and 50% smaller than the assumed pseudo network of 18 seismic stations (Figure S6 in Supporting Information S1). Besides, the distribution of E_1 around the optimal source location A depends on the source mechanism. The misfit distribution expanding toward north-west direction in our result (Figure 6a) may reflect the source mechanism.

We thus compare the source mechanisms expressed as eigenvectors of the moment tensors between the input source models and the output solutions (Figure S7 in Supporting Information S1). Results show that source mechanisms are not so well constrained in the case of our very-near-field seismic network. Comparing the principal axes and the eigenvalues of the solutions, the very-near-field network may not be more appropriate to determine the source mechanisms than distant networks, as has been already discussed by the resolution matrix in Section 5.1. The resolution of the moment tensors for the pseudo network is slightly better, but there is still a trade-off especially for the M_{zz} component. Hence, we conclude that topography at Stromboli is limiting the geometry of the seismic network and therefore the moment tensor solution are in general not well constrained and may not be used for a detailed discussion on source mechanisms (Figure S8 in Supporting Information S1 and Appendix C).

5.3. Semblance Analysis

Reliability of the source location derived by semblance analysis is a priority to understand how realistic the migration of the source inferred for the different phases identified in the VLP1 frequency band before (Preeding phase), during (Main phase1) and after (Main phase2) the explosive onset. Since seismic wavelength is in the order of tens of kilometers, semblance, in theory, does not seem to have the required spatial resolution to constrain the source location. Therefore, we perform semblance analysis using synthetic seismograms by assuming an isotropic expansion/contraction source with two different locations at 50 m away from each other.

The spatial distribution of S_3 obtained by grid search (Figure 12) indicates how well the source location is constrained. Figure 12a shows the contour lines of S_3 around the optimal source locations of Preceding phase and Main phase1 for a typical VLP1 event. The contour lines are interpolated at the same intervals in the regions smaller than source grid interval (25 m). The semblance values gradually decrease with distances from the optimal source locations because of the long-period nature of the analyzed seismic waves. As a consequence,
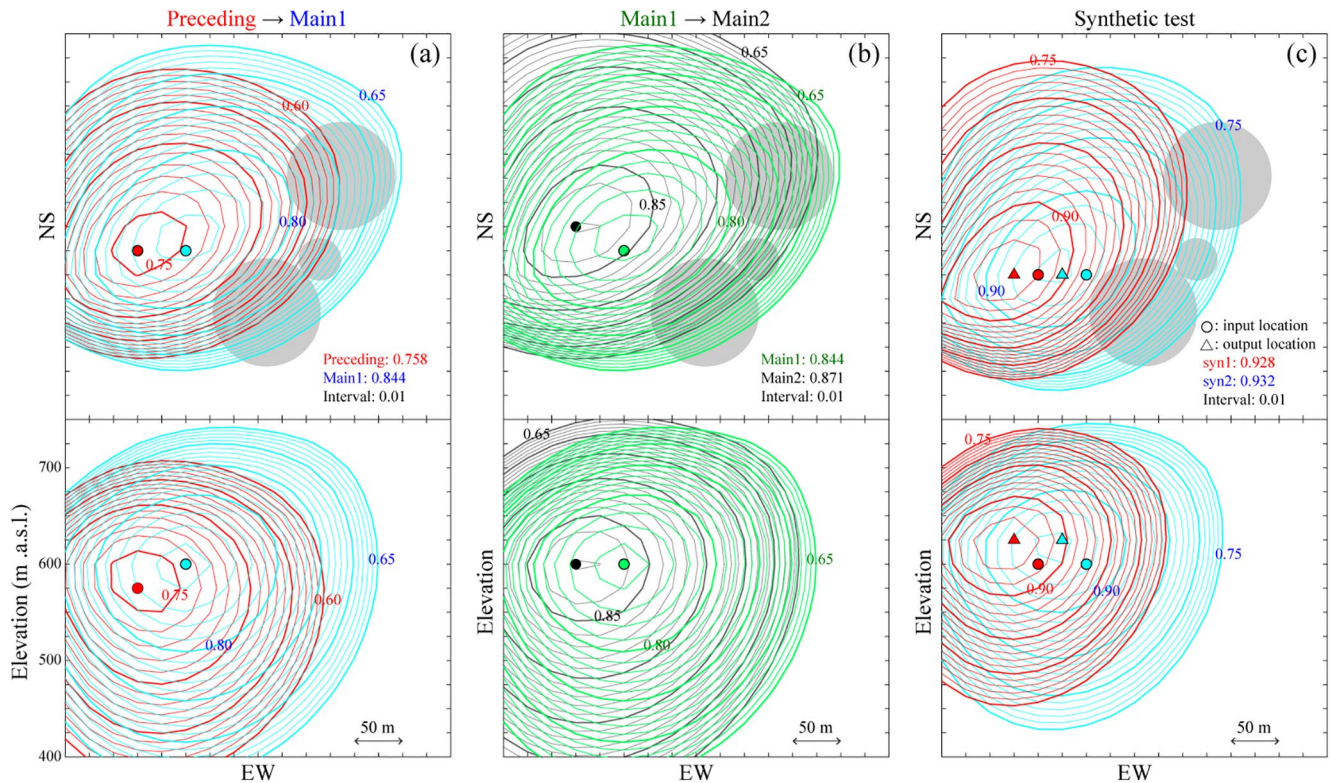
Figure 12. (a) Map distribution of semblance (S_3) around the optimal source location of the Preceding phase (red) and Main phase1 (light blue) for the seismic event occurred at 18:43 on 26 September 2016. The NE, C and SW craters are shown by gray circles. Semblance of the source locations are listed at the lower right corner of the horizontal panel. The contour lines are drawn with an interval of 0.01. (b) Map of the semblance distribution, S_3 calculated for the Main phase1 (light green) and Main phase2 (black) of the real seismic signal and (c) of the synthetic test. Two input source locations are shown by the red and light blue dots. The estimated locations are represented by the red and light blue triangles.

semblance close to the optimal source location shows high values and the difference between the source locations for the three phases is not so large. The semblance values for Main phase1 and Main phase2 show also similar characteristics.

We then apply the same analysis to the pseudo VLP1 phase to understand the effects of network configuration, travel times and wave propagation on the semblance analysis. The result of this test shows semblance (S_3) of 0.928 and 0.932, for both sources located only 50 m apart, respectively. When we overlap the S_3 contour lines obtained for the two source locations we get a distribution similar to the real VLP. Our test shows (Figure 12c) similar results both when synthetic full-waveforms or in several time windows are used. Contrary to what expected, this strongly suggests that semblance analysis can well determine source location difference as small as 50 m and that the obtained source migration of several tens of meters is plausible. The absolute locations are estimated to be one grid (25 m) west of and above the modeled sources (Figure 12c), and such difference may be caused by the station coverage around the source and by the effect of topography on wave propagation.

Finally, we verify the reliability of the eastward source migration before an explosion (Figure 10a) by measuring the arrival time difference between the Preceding phase (t_0) and Main phase1 (t_1) at the ST4 and ST5 seismic stations. Time differences were estimated by cross-correlation using a 4-s-long time window centered around the maximum amplitude recorded in the two phases (Figure 13a). Considering the location of these two stations, the time difference $(t_1 - t_0)^{ST4} - (t_1 - t_0)^{ST5}$ is expected to be positive when the source migrates eastward. Although the wavelength is so large to make difficult to measure time delays with high accuracy, we found that, as predicted, time delays are positive (Figure 13b).

In conclusion, we believe that the reliability of the source location using six different methods has been largely demonstrated. All the different methods show that different frequency band (VLP1, VLP2, and LP) have different locations and that the seismic source of the VLP1 migrates with time in the east-west direction. Even if absolute
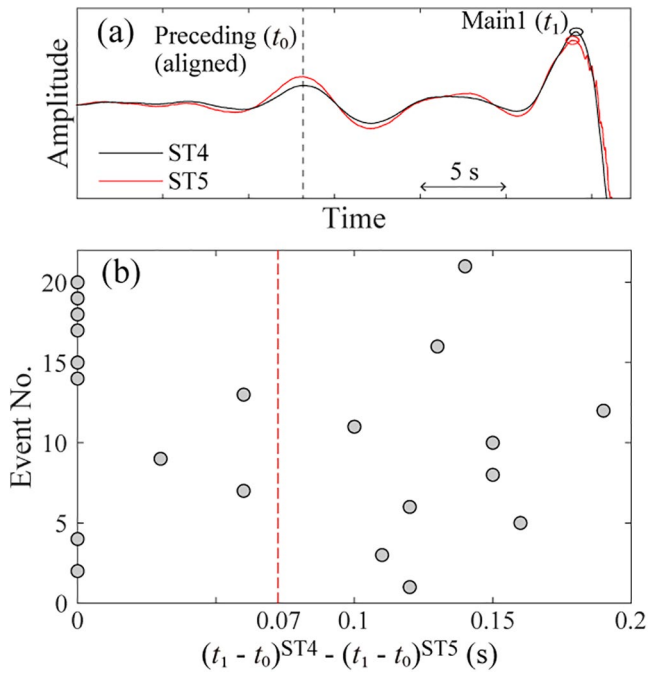
Figure 13. (a) Example of the Preceding phase and Main phase1 recorded at ST4 (black) and ST5 (red) seismic stations. Waveforms are aligned according to the occurrence of the Preceding phase (t_0). Circles on the Main phase1 show the position of the maximum amplitudes. (b) Measured time delays $\left(t_1 - t_0\right)^{ST4} - \left(t_1 - t_0\right)^{ST5}$ for the 21 seismic events in which Preceding phase is detected. The positive time delay suggests eastward source migration. The dashed line represents the average time delay for the 21 events.

location strongly depends on focal mechanisms, the relative locations are very reliable (<50 m) for a given source and thus temporal migration of the source using the semblance method is reliable and significant.

6. Discussion

6.1. Source Migration

Since the moment tensor inversion strongly reflects the source location and the mechanism of the large seismic amplitudes, the centroid of VLP1 mainly represents the location where seismic waves are excited after the explosion onset. On the other hand, VLP2 and LP frequency band are related to the seismic waves excited almost at the same time of the explosion. This means that the source location of VLP1 coincides with the Main phase2 while source locations of VLP2 and LP are associated with the Main phase1. Eastward migration of the source is revealed by the moment tensor inversion and by the semblance analysis. Relative distances between the position of the seismic source responsible for the VLP1, VLP2, and LP frequency bands are almost the same and very close to the Preceding phase, Main phase1 and Main phase2. Since semblance analysis assumes an isotropic source mechanism, source location derived by the moment tensor inversions which is independent by the source mechanisms has to be considered as more reliable. We correct the source location of the Preceding phase by considering the offsets derived by the two different methodology, and we infer that the seismic source migrates mostly in the east-west 10–20 s before an explosion. The first source (Preceding phase) is located about 150 m west of the craters, just before or at the explosion onset, source is located beneath the craters and after the eruption onset, the source moves back to the west of the craters in the same location of the Preceding phase.

Downward migration of the VLP source was described also by Rowe et al. (1998) as associated with gas bubble bursts in basaltic magma at Erebus volcano. They interpret spectral peaks at periods of 7, 10, and 20 s of VLP seismic signal as a fundamental mode with the two overtones caused by the resonance of magma reservoir/conduit or nonlinear fluid-flow excitation. Seismic signal at Stromboli also shows spectral peaks at periods of 3.7, 5, and 10 s (Figure 3b). Since these can be interpreted as a fundamental mode (10 s) with two overtones (5 and 3.7 s), the westward source migration following the explosions may be interpreted as the resonance process due to the propagation of pressure waves and/or fluid flow in the magma reservoir/conduit system. Although the physical parameters to represent the resonance process such as sound velocity and conduit dimensions are not estimated in this study, our observation suggests the existence of a finite-size pressure source.

6.2. Amplitude and Temporal Characteristics of VLP Seismic Phases

To understand the origin of the Preceding phase and its link to eruption dynamics, we consider the peak amplitude and its occurrence in time (a_0, t_0) of the 21 seismic signals with the best signal-to-noise ratio and we then calculate the cross correlation with amplitude of the Main phase1 (a_1), of the Main phase2 (a_2), of the raw seismic signal (a_3) and of the acoustic signal (a_4) recorded at the ST1 station (Table 1 and Figure S9 in Supporting Information S1). Besides, amplitudes of this different phases were compared with the time delay ($t_1 - t_0$) between the maximum amplitudes of the Main phase1 (t_1) and of the Preceding phase (t_0).

We found that the higher correlation ($R = 0.8$) is between the amplitude of the raw seismic signal (a_3) and the amplitude of the acoustic signal (a_4). This correlation supports the evidence (Figure 14e) that amplitude of the seismic signal is highly controlled by the flux of gas and lapilli outside the vent during the explosive mechanism. In addition, amplitude of the Preceding phase (a_0) well correlates ($R = 0.68$) with the amplitude of the Main phase1 (a_1) (Figure 14c), which seems indicating that the small seismic signal generated 10–20 s before the explosion (Preceding phase), probably by the magma/gas movement inside the conduit (see Ripepe, Delle Donne,

Table 1
Correlation Coefficients Between the Measured Amplitude and Onset Time Parameters of Seismic and Acoustic Signals

	Time difference $t_1 - t_0$	Preceding phase a_0	Main phase1 a_1	Main phase2 a_2	Raw seismic signal a_3	Raw acoustic signal a_4
$t_1 - t_0$		−0.18	−0.06	−0.11	**0.26**	0.12
a_0			**0.64**	0.36	0.27	**0.34**
a_1				0.56	0.16	0.22
a_2					0.39	0.48
a_3						**0.80**
a_4						

Note. The pairs with a cell written in bold are shown in Figure 14, and the others are in Figure S9 in Supporting Informarion S1.

et al., 2021), is somehow proportional to the magnitude/strength of the explosion itself (Main phase1). Since the amplitude of Main phase2 (a_2) is only little correlated ($R = 0.48$) to the acoustic amplitude (a_4), it is not clear where the explosive dynamics at the magma surface is responsible or not for the origin of the oscillations of the ground occurring after the explosion. No relation is found between the duration ($t_1 - t_0$) of the Preceding phase and the considered amplitudes (Table 1).

6.3. Conceptual Model of the Explosion at Stromboli

Based on these results, we suggest here a possible magma dynamics acting for several tens of seconds before and after the explosive eruptions at Stromboli volcano. Geometry of the assumed feeding system is based on previous
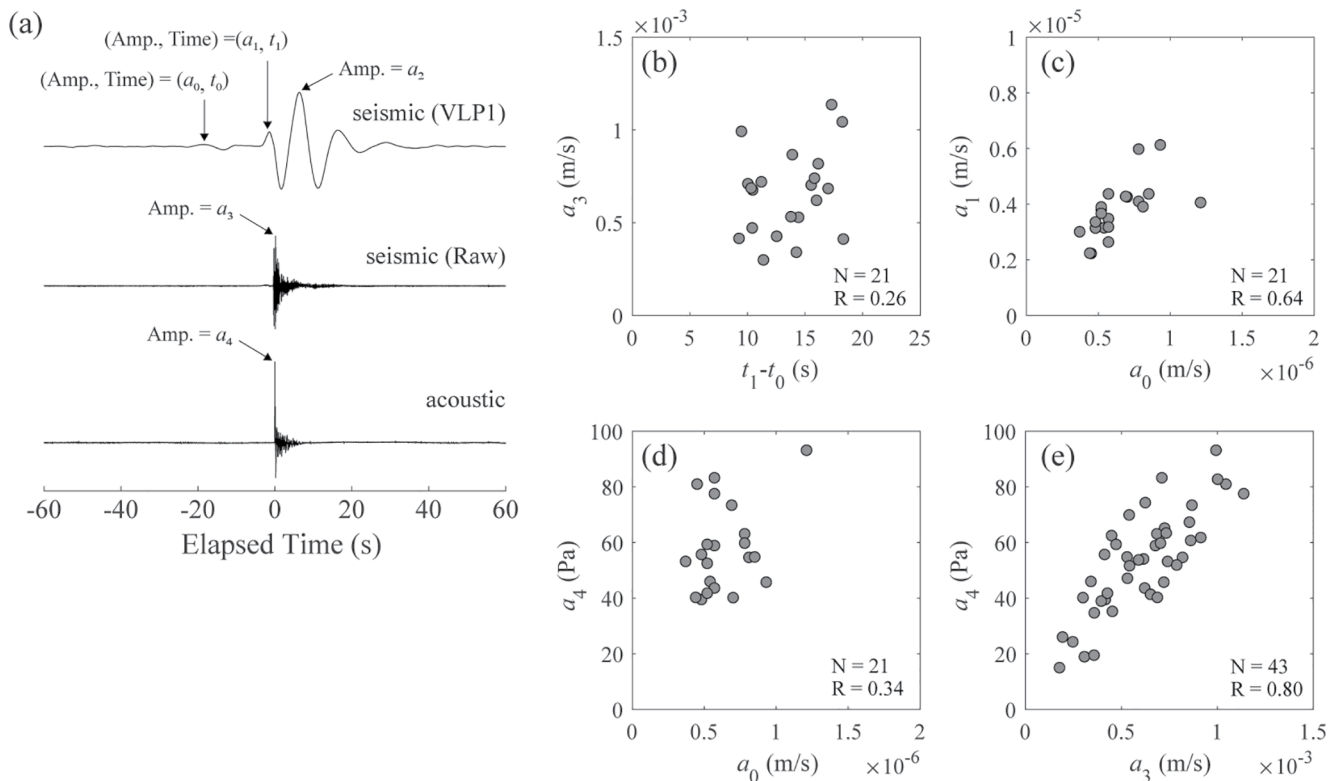
Figure 14. (a) Example of seismic and acoustic signals recorded at ST1. Peak amplitudes and occurrence times of the Preceding phase (a_0, t_0) and of the Main phase1(a_1, t_1), the peak amplitude of Main phase2 (a_2), the peak amplitude of the raw seismic signal (a_3) and the amplitude of acoustic signal (a_4) are shown. (b) Relationship between the time difference ($t_1 - t_0$) and the amplitude of raw seismic signal (a_3). The decision (correlation) coefficient (R) and the number of analyzed events (N) are displayed in the lower right of the panel. (c) The amplitudes of the Preceding phase (a_0) and the Main phase1 (a_1). (d) The amplitudes of the Preceding phase (a_0) and raw acoustic signal (a_4). (e) The amplitudes of raw seismic signal (a_3) and raw acoustic signal (a_4).

models derived to explain magma degassing (Suckale et al., 2016), effusive eruptions (Ripepe et al., 2015, 2017; Valade et al., 2016) and ground deformation (Ripepe, Lacanna, et al., 2021).

The west-to-east migration of the seismic source before (Preceding phase), during (Main phase1) and after (Main phase2) the explosive eruption is suggesting that the feeding system is bending toward northeast in the last few hundreds of meters before the surface. This result is in agreement with the migration of the VLP seismicity observed during the effusive eruptions (Giudicepietro et al., 2009; Ripepe et al., 2015; Valade et al., 2016) when the back azimuth of the VLPs moves deeper and westward following the lowering of the magma level in the shallow feeding system.

Our conceptual model is considering seismic VLP as part of the slow ground inflation (Genco & Ripepe, 2010; Ripepe, Delle Donne, et al., 2021) that starts about 150–200 s before the explosion onset (Figure 15a). This inflation is explained as generated by the pressure increase due to the accumulation of gas-rich magma below a crystal-rich and dense magma mush (Suckale et al., 2016) acting as a "cap" for the gas (Ripepe, Delle Donne, et al., 2021) and pushing up the last (150–200 m) of magma column.

About 10–20 s before the onset of explosion, the ground inflation rate increases ∼10 times as the gas gets closer to the surface (Genco & Ripepe, 2010). Reaching the surface gas flux accelerates, generating a pressure source that excites small seismic waves (Preceding phase, Figure 15b). About 5 s before the explosion onset (Figure 15c), the pressure source moves eastward to the crater, exciting the Main phase1 in the VLP1 frequency band and the LP seismic waves. The eastward migration of the source is most probably reflecting the geometry of the shallow feeding system which is bending toward northeast in the last 120–170 m below the surface.

When the explosion occurs (Figure 15d), large seismic waves in the VLP2 and LP frequency component of the seismic spectrum are excited below the crater and associated with acoustic waves (e.g., Chouet et al., 1997; Harris & Ripepe, 2007; Ripepe et al., 2001). After the explosion, seismic source (Main phase2) migrates back toward west almost to the same location of the Preceding phase (Figure 15e). This migration is most probably caused by a resonance process which induces the oscillation of the upper part of the magma column while is recovering the equilibrium after the explosive magma/gas released (Ripepe, Delle Donne, et al., 2021).
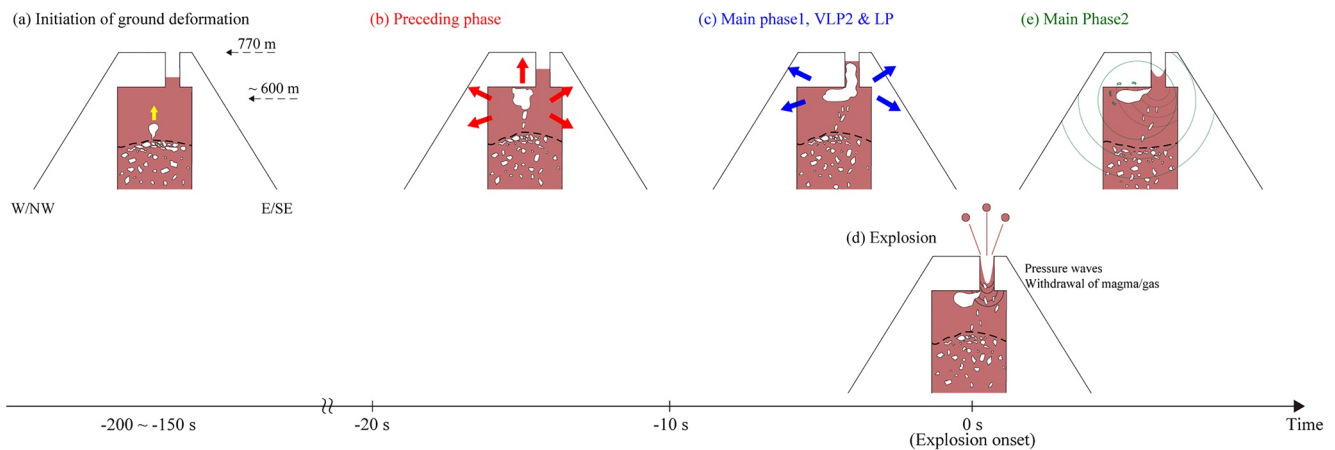
Figure 15. Schematic illustration of explosion process at Stromboli volcano as inferred from the seismic source. (a) About 150–200 s before the explosion onset, ground inflation starts due to the pressure increase caused by the accumulation of gas-rich magma below a crystal-rich and dense magma mush and the gas pushing up the magma column. (b) About 10–20 s before, the acceleration of magma and/or gas bubble motions beneath the crater generates small seismic waves (Preceding phase). (c) From about 5 s before the explosion onset, the pressure source moves eastward to the crater along the geometry of the shallow feeding system, exciting VLP1 and VLP2 seismic waves (Main phase1) and LP seismic waves. (d) Explosion occurs and generates large seismic waves and acoustic waves. (e) The pressure source migrates westward and then moves back to almost the same location of Preceding phase, exciting large and resonant VLP1 seismic waves (Main phase2). See detail in text.

7. Conclusions

We have examined seismic signals generated by small explosive eruptions at Stromboli volcano recorded at only 100–300 m away from the active craters. Large amplitude of VLP and long-period (LP) signals mainly occur during and after the explosive onset and are thus reflecting by the explosive dynamics. We show for the first time that small amplitude seismic signal in the 0.05–0.2 Hz (VLP1) frequency band is detected 10–20 s prior (Preceding phase) the explosive onset. This is the seismic response of the sharp ground acceleration occurring at the end of the 150–200 s long inflation cycle associated with each explosion at Stromboli volcano (Genco & Ripepe, 2010; Ripepe, Delle Donne, et al., 2021).

Moment tensor inversion reveals that the source of the large VLP1 (0.05–0.2 Hz) amplitude is located around the edge of the southwest (SW) crater at an elevation of 600 m a.s.l. This location does not coincide with the explosive vent, but is 150–200 m southwest of NE crater where explosion are located by acoustic waves. In agreement with previous observation (Ripepe, Delle Donne, et al., 2021), we infer that the large amplitude seismic VLP1 frequency band is excited in the very shallow portion of the magma conduit and is probably caused by a reaction force related to the withdrawal of magma/gas during the explosive eruption. This interpretation finds an evidence in the source mechanisms which is dominated by the vertical dipole component of the moment tensor.

At higher frequency band, seismic sources associated with VLP2 (0.2–0.5 Hz) and LP (0.5–1.0 Hz) spectral component are located almost beneath the NE crater. Their location coincide then with the exploding vent and are excited at the explosion onset. Semblance analysis of the small Preceding phase and of the Main phase reveals that the pressure source moves back and forth from the western side of the crater area to the east below the exploding crater. This migration of the seismic source is in agreement also with the source locations estimated by moment tensor solution, and seems tracking the movement of the gas-rich magma batch during the last tens of second before the explosion. East-to-west movement of the relative location of VLPs has been at Stromboli also observed during lateral effusive eruption and have been explained as following the lowering of the magma level during the drainage of the magma from the very shallow portion of the magma reservoir (Ripepe et al., 2015; Valade et al., 2016). We suggest that migration of VLPs is controlled by the geometry of the shallow feeding conduit located beneath the crater terrace which is bending from the southwest toward the northeast following the main structural feature of the volcano edifice.

Appendix A: Moment Tensor Inversion Including Tilt Motions: Method and Computation System

Observed seismogram generated by a point source moment-tensor can be represented in the frequency domain as

$$U_n^{\text{obs}}(\omega) = M_{pq}(\omega)\left[G_{np,q}^{\text{trans}}(\omega)I_n^{\text{trans}}(\omega) + G_{np,q}^{\text{tilt}}(\omega)I_n^{\text{tilt}}(\omega) \right], \tag{A1}$$

where ω is the angular frequency, $U_n^{\text{obs}}(\omega)$ is the Fourier spectrum of the observed seismogram, n represents the component, $M_{pq}(\omega)$ is the Fourier spectrum of the moment tensor with pth direction of the force and qth direction of the arm of the moment, $G_{np,q}^{\text{trans}}(\omega)$ and $G_{np,q}^{\text{tilt}}(\omega)$ are the Fourier spectra of Green's functions for translational and tilt motions, respectively, and $I_n^{\text{trans}}(\omega)$ and $I_n^{\text{tilt}}(\omega)$ are the seismometer's responses to translational and tilt motions, respectively. The tilt response in a seismometer for the horizontal and vertical components can be represented as

$$I_n^{\text{tilt}}(\omega) = \begin{cases} \dfrac{g}{(i\omega)^2}I_n^{\text{trans}}(\omega) & \text{for horizontal components} \\ 0 & \text{for vertical component} \end{cases}, \tag{A2}$$

where g is the gravitational acceleration and i is the imaginary unit. The detailed derivation of Equation A2 is described in Aoyama (2008) and Maeda et al. (2011).

The matrix form of Equation A1 incorporating Equation A2 can be written as

$$d = Gm, \tag{A3}$$
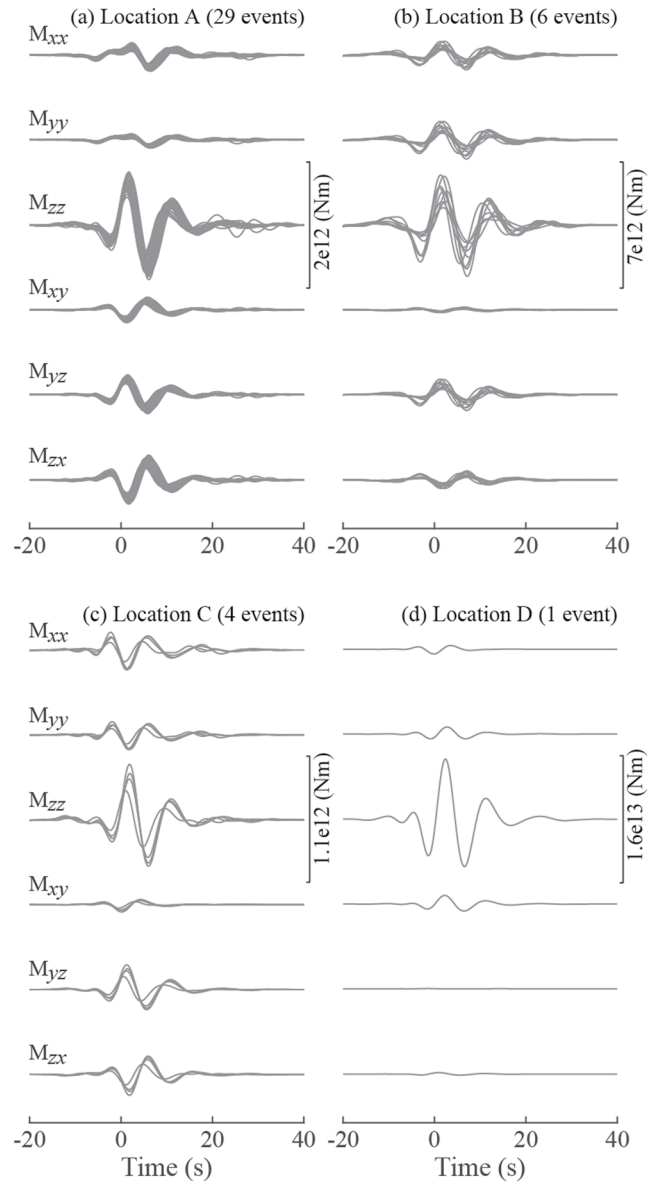
Figure A1. Moment tensor solutions of the 43 events. The solutions are plotted together for the events located at (a) Location A, (b) Location B, (c) Location C, and (d) Location D.

where G is the matrix consisting of the Green's functions and response functions for both translational and tilt motions, d is the seismic data vector and m represents the source mechanism vector that consists of six moment tensors. The least squares solution of the source mechanism is written as

$$m^{\mathrm{s}} = \left[G^{\mathrm{H}} G \right]^{-1} G^{\mathrm{H}} d, \tag{A4}$$

where the symbol $^{\mathrm{H}}$ indicates the conjugate transpose (Hermitian). The synthetic seismograms are obtained by the inverse Fourier transform of the product of the Green's functions G and the solution m^{s}. In this method, the tilt effect is included in the Green's function term so that the decomposition of the observed seismogram into translational and tilt contributions is not required.
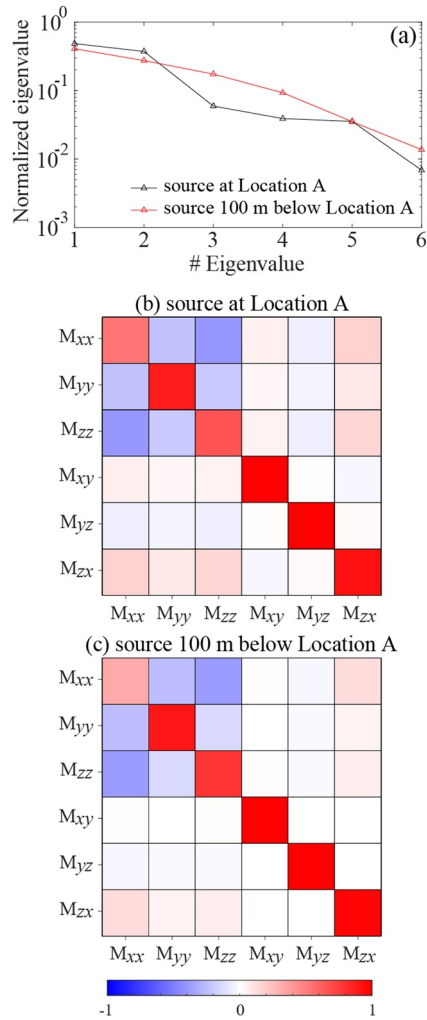
Figure A2. (a) Distribution of eigenvalues obtained by the singular value decomposition of the Green's functions computed from the point source at Location A (black) and the one 100 m below Location A (red). (b) Model resolution matrix calculated when the source location is Location A. (c) Model resolution matrix calculated when the source location is 100 m below Location A. The color scale indicates the value of resolution.

The Green's functions are convolved with a cosine function to stabilize the inversion:

$$S(t) = \begin{cases} \dfrac{1}{2}\left[1 - \cos\left(\dfrac{2\pi t}{t_r}\right)\right], & 0 \le t < t_r, \\ 0, & t \ge t_r \end{cases} \tag{A5}$$

where t_r, is the rising time of the source time function. To obtain the moment tensor solution independent of the assumed source time function, this cosine function is also convolved into the data vector that consists of the observed seismograms.

Our computational domain consists of a grid with $401 \times 401 \times 201$ nodes in the north-south (NS), east-west (EW) and up-down (UD) directions equispaced by 10 m for a total length of $4 \times 4 \times 2$ km. The center of the domain is set at the summit. Positive x and y directions are set to be north and east, respectively, and z direction is vertical one with downward positive. This Cartesian coordinate is based on the computational one in OpenSWPC. The Perfectly Matched Layer (PML) boundary condition (Chew & Liu, 1996) is adopted to minimize artificial reflections. Note that the output waveform is changed to be upward positive in this software. First, the Green's functions for translational motion $G_{np,q}^{\text{trans}}(\omega)$ are yielded at the eight broadband seismic stations by convolving

the cosine function in Equation A5 with $t_r = 0.5$ s. We calculate the Green's functions in velocity response and use the observed velocity seismograms for the data vector $\boldsymbol{d}$. This is because the Green's functions include static offset in displacements due to near-field term, which may lead to phase reversal in the time function of $\boldsymbol{m}^s$ due to the cyclic convolution. Subsequently, we calculate the Green's functions for tilt motion $G_{np,q}^{\text{tilt}}(\omega)$ by computing the vertical displacement at the grids around the stations with 10 m interval, taking the difference of the vertical displacements in the NS and EW directions, and converting to the velocity responses.

Appendix B: Source Mechanisms of the 43 Events for VLP1 Signal

Figure A1 shows the moment tensor solutions for the 43 events whose locations are determined at the four locations (Location A-D) in Figure 9a. The vertical dipole component is dominant for all the four source locations. The moment tensor source time functions at Location A, B and C, which are located within 50 m (1 grid), are well matched with each other. Carefully looking at the moment tensor solutions, we may see slight differences: For example, M_{xx} and M_{yy} at Location A show slightly different temporal changes compared with those at Locations B and C; Amplitudes of the moment tensor solutions at Locations A and C are almost same among different events, while those at Location B seem to be scattered. On the other hand, the moment tensors at Location D show larger amplitude in the M_{zz} component. However, only 1 event is determined at Location D. Hence, we may not discuss the detail of the difference from the moment tensors at the other locations.

Appendix C: Model Resolution Matrices

The model resolution matrices are calculated from the singular-value decomposition of the Green's functions and the generalized inverse of them. Figure A2a shows the distribution of eigenvalues obtained from the singular-value decomposition of the data kernel that consists of the Green's functions computed from the point source at Location A (Figure 9a) and the one 100 m below Location A. The point source 100 m below Location A is selected to examine the depth dependence of the resolution. This depth is consistent with the result of VLP source locations determined by some previous studies (e.g., Chouet et al., 2003; Marchetti & Ripepe, 2005). The smallest eigenvalues for the two source depths are sufficiently small to the other eigenvalues: the smallest eigenvalues at the two depths are 0.69% and 1.37% of overall contribution, respectively. Here, we place the smallest eigenvalues with zero to consider the pseudoinverse problem. The model resolution matrices for the two source locations are shown in Figures A2b and A2c. The result in Figure A2b shows that the resolution of the diagonal components of the moment tensors (M_{xx}, M_{yy}, and M_{zz}) are lower than the deviatoric ones (M_{xy}, M_{yz}, and M_{zx}): the resolutions of the diagonal components range from 0.54 to 0.88, and those of the deviatoric components from 0.93 to 0.99. The covariances of the diagonal components range from −0.39 to −0.20 and those of the deviatoric components from −0.02 to 0.02. These results indicate that there are large trade-offs between one diagonal moment tensor and the other two diagonal ones, although trade-offs between the deviatoric tensors and the diagonal ones are small. That is, the diagonal components of the moment tensors are not very well constrained even when using our very-near-field observation data. On the other hand, the well-constrained deviatoric components indicate the dominance of the diagonal components in the source mechanism. The model resolution matrix for the deeper source (Figure A2c) shows that the resolution of the diagonal components of the moment tensors is estimated to be 0.33, 0.90, and 0.79, respectively. Although the contribution of the smallest eigenvalue to the mechanism solution and the resolution of M_{zz} for the deeper source are higher than those for Location A, we may not be able to discuss the differences of source mechanism such as crack, cylindrical and spherical pressure source.

We calculate the model resolution matrices using the Green's functions computed at the pseudo seismic network (Figure S5 in Supporting Informarion S1) and compare them with the results of the very-near-field network. Distribution of eigenvalues obtained by the singular value decomposition of the Green's functions is shown in Figure S8a in Supporting Informarion S1. For Location A, the smallest eigenvalue is 1.49% of overall contribution. For the source 100 m below Location A, the smallest eigenvalue is 2.47% of overall contribution. These results show that the smallest eigenvalues contribute to the mechanism solutions compared with the case of the very-near-field network. When we place the smallest eigenvalues with zero to consider the pseudoinverse problem, the model resolution matrices show the trade-offs between one diagonal moment tensor and the other two diagonal ones (Figures S8b and S8c in Supporting Informarion S1): the resolution of the diagonal components of the moment tensors is estimated to be 0.76, 0.87, and 0.45, respectively in the case of Location A, and 0.62, 0.80, and 0.64

in the case of the deeper source. Although the contribution of the smallest eigenvalue to the mechanism solution and the resolution of M_{xx} are improved by the pseudo seismic network, the results suggest that further ingenuity in network configuration will be necessary to improve the inversion solutions for understanding the volumetric changes in detail.

Data Availability Statement

The authors comply with AGU's data policy and the seismic and acoustic data are available through the Zenodo online repository (http://doi.org/10.5281/zenodo.4082042).

References

Aoyama, H. (2008). Simplified test on tilt response of CMG40T seismometers (in Japanese with English abstract). *Bulletin of the Volcanological Society of Japan*, *53*, 35–46.

Auger, E., D'Auria, L., Martini, M., Chouet, B., & Dawson, P. (2006). Real-time monitoring and massive inversion of source parameters of very long period seismic signals: An application to Stromboli Volcano, Italy. *Geophysical Research Letters*, *33*(4), L04301. https://doi.org/10.1029/2005gl024703

Barth, A., Edmonds, M., & Woods, A. (2019). Valve-like dynamics of gas flow through a packed crystal mush and cyclic Strombolian explosions. *Scientific Reports*, *9*, 821. https://doi.org/10.1038/s41598-018-37013-8

Batchelor, G. K. (1967). *An introduction to fluid dynamics*. Cambridge University Press.

Blackburn, E. A., Wilson, L., & Sparks, R. S. J. (1976). Mechanics and dynamics of Strombolian activity. *Journal of the Geological Society*, *132*(4), 429–440. https://doi.org/10.1144/gsjgs.132.4.0429

Chew, W. C., & Liu, Q. H. (1996). Perfectly matched layers for elastodynamics: A new absorbing boundary condition. *Journal of Computational Acoustics*, *4*(4), 341–359. https://doi.org/10.1142/S0218396X96000118

Chouet, B., Dawson, P., Ohminato, T., Martini, M., Saccorotti, G., Giudicepietro, F., et al. (2003). Source mechanisms of explosions at Stromboli Volcano, Italy, determined from moment-tensor inversions of very-long-period data. *Journal of Geophysical Research*, *108*(B1). https://doi.org/10.1029/2002JB001919

Chouet, B., De Luca, G., Milana, G., Dawson, P., Martini, M., & Scarpa, R. (1998). Shallow velocity structure of Stromboli Volcano, Italy, derived from small-aperture array measurements of Strombolian tremor. *Bulletin of the Seismological Society of America*, *88*(3), 653–666.

Chouet, B., Saccorotti, G., Martini, M., Dawson, P., De Luca, G., Milana, G., & Scarpa, R. (1997). Source and path effects in the wavefields of tremor and explosions at Stromboli Volcano, Italy. *Journal of Geophysical Research*, *102*(B715), 15129–15150. https://doi.org/10.1029/97JB00953

Del Bello, E., Llewellin, E. W., Taddeucci, J., Scarlato, P., & Lane, S. J. (2012). An analytical model for gas overpressure in slug-driven explosions: Insights into Strombolian volcanic eruptions. *Journal of Geophysical Research*, *117*(B2), B02206. https://doi.org/10.1029/2011JB008747

Genco, R., & Ripepe, M. (2010). Inflation-deflation cycles revealed by tilt and seismic records at Stromboli volcano. *Geophysical Research Letters*, *37*(12), L12302. https://doi.org/10.1029/2010GL042925

Giudicepietro, F., D'Auria, L., Martini, M., Caputo, T., Peluso, R., De Cesare, W., et al. (2009). Changes in the VLP seismic source during the 2007 Stromboli eruption. *Journal of Volcanology and Geothermal Research*, *182*(3–4), 162–171. https://doi.org/10.1016/j.jvolgeores.2008.11.008

Gurioli, L., Colo, L., Bollasina, A., Harris, A. J., Whittington, A., & Ripepe, M. (2014). Dynamics of Strombolian explosions: Inferences from field and laboratory studies of erupted bombs from Stromboli volcano. *Journal of Geophysical Research*, *119*(1), 319–345. https://doi.org/10.1002/2013JB010355

Harris, A. J. L., & Ripepe, M. (2007). Synergy of multiple geophysical approaches to unravel explosive eruption conduit and source dynamics—A case study from Stromboli. *Chemie der Erde*, *67*(1), 1–35. https://doi.org/10.1016/j.chemer.2007.01.003

Ishii, K., Yokoo, A., Kagiyama, T., Ohkura, T., Yoshikawa, S., & Inoue, H. (2019). Gas flow dynamics in the conduit of Strombolian explosions inferred from seismo-acoustic observations at Aso volcano, Japan. *The Earth, Planets and Space*, *71*(1), 1–15. https://doi.org/10.1186/s40623-019-0992-z

James, M. R., Lane, S. J., Chouet, B., & Gilbert, J. S. (2004). Pressure changes associated with the ascent and bursting of gas slugs in liquid filled vertical and inclined conduits. *Journal of Volcanology and Geothermal Research*, *129*(1–3), 61–82. https://doi.org/10.1016/s0377-0273(03)00232-4

James, M. R., Lane, S. J., & Corder, S. B. (2008). Modelling the rapid near-surface expansion of gas slugs in low-viscosity magmas. In S. J. Lane, & J. S. Gilbert (Eds.), *Fluid motions in volcanic conduits: A source of seismic and acoustic signals* (Vol. 307, pp. 147–167). Geological Society, London, Special Publications. https://doi.org/10.1144/sp307.9

James, M. R., Lane, S. J., Wilson, L., & Corder, S. B. (2009). Degassing at low magma-viscosity volcanoes: Quantifying the transition between passive bubble-burst and Strombolian eruption. *Journal of Volcanology and Geothermal Research*, *180*(2–4), 81–88. https://doi.org/10.1016/j.jvolgeores.2008.09.002

Jaupart, C., & Vergniolle, S. (1988). Laboratory models of Hawaiian and Strombolian eruptions. *Nature*, *331*(6151), 58–60. https://doi.org/10.1038/331058a0

Jaupart, C., & Vergniolle, S. (1989). The generation and collapse of a foam layer at the roof of a basaltic magma chamber. *Journal of Fluid Mechanics*, *203*, 347–380. https://doi.org/10.1017/S0022112089001497

Kawaguchi, R., & Nishimura, T. (2015). Numerical investigation of temporal changes in volcanic deformation caused by a gas slug ascent in the conduit. *Journal of Volcanology and Geothermal Research*, *302*, 1–10. https://doi.org/10.1016/j.jvolgeores.2015.06.002

Kawakatsu, H., Kaneshima, S., Matsubayashi, H., Ohminato, T., Sudo, Y., Tsutsui, T., et al. (2000). Aso94: Aso seismic observation with broadband instruments. *Journal of Volcanology and Geothermal Research*, *101*(1–2), 129–154. https://doi.org/10.1016/S0377-0273(00)00166-9

Lacanna, G., & Ripepe, M. (2020). Modeling the acoustic flux inside the magmatic conduit by 3D-FDTD simulation. *Journal of Geophysical Research*, *125*, e2019JB018849. https://doi.org/10.1029/2019JB018849

Levander, A. R. (1988). Fourth-order finite-difference P-SV seismograms. *Geophysics*, *53*(11), 1425–1436. https://doi.org/10.1190/1.1442422

Llewellin, E. W., Del Bello, E., Taddeucci, J., Scarlato, P., & Lane, S. J. (2012). The thickness of the falling film of liquid around a Taylor bubble. *Proceedings of the Royal Society A: Mathematical, Physical and Engineering Sciences*, *468*(2140), 1041–1064. https://doi.org/10.1098/rspa.2011.0476

Maeda, T., Takemura, S., & Furumura, T. (2017). OpenSWPC: An open-source integrated parallel simulation code for modeling seismic wave propagation in 3D heterogeneous viscoelastic media. *Earth, Planets and Space*, *69*(1), 102. https://doi.org/10.1186/s40623-017-0687-2

Maeda, Y., Takeo, M., & Ohminato, T. (2011). A waveform inversion including tilt: Method and simple tests. *Geophysical Journal International*, *184*(2), 907–918. https://doi.org/10.1111/j.1365-246X.2010.04892.x

Marchetti, E., & Ripepe, M. (2005). Stability of the seismic source during effusive and explosive activity at Stromboli Volcano. *Geophysical Research Letters*, *32*(3), L03307. https://doi.org/10.1029/2004GL021406

Martini, M., Giudicepietro, F., D'Auria, L., Esposito, A. M., Caputo, T., Curciotti, R., et al. (2007). Seismological monitoring of the February 2007 effusive eruption of the Stromboli volcano. *Annals of Geophysics*, *50*(6), 775–788.

Menke, W. (1984). *Geophysical data analysis: Discrete inverse theory*. Academic Press, Inc.

Neri, M., & Lanzafame, G. (2009). Structural features of the 2007 Stromboli eruption. *Journal of Volcanology and Geothermal Research*, *182*(3–4), 137–144. https://doi.org/10.1016/j.jvolgeores.2008.07.021

Ohminato, T., Chouet, B. A., Dawson, P. B., & Kedar, S. (1998). Waveform inversion of very-long-period impulsive signals associated with magmatic injection beneath Kilauea Volcano, Hawaii. *Journal of Geophysical Research*, *103*(B1023),23839–23862. https://doi.org/10.1029/98JB01122

Parfitt, E. A. (2004). A discussion of the mechanisms of explosive basaltic eruptions. *Journal of Volcanology and Geothermal Research*, *134*(1–2), 77–107. https://doi.org/10.1016/j.jvolgeores.2004.01.002

Patanè, D., Barberi, G., De Gori, P., Cocina, O., Zuccarello, L., Garcia-Yeguas, A., et al. (2017). The shallow magma chamber of Stromboli Volcano (Italy). *Geophysical Research Letters*, *44*(13), 6589–6596. https://doi.org/10.1002/2017GL073008

Ripepe, M. (1996). Evidence for gas influence on volcanic seismic signals recorded at Stromboli. *Journal of Volcanology and Geothermal Research*, *70*(3–4), 221–233. https://doi.org/10.1016/0377-0273(95)00057-7

Ripepe, M., Ciliberto, S., & Della Schiava, M. (2001). Time constraints for modeling source dynamics of volcanic explosions at Stromboli. *Journal of Geophysical Research*, *106*(B5), 8713–8727. https://doi.org/10.1029/2000JB900374

Ripepe, M., Delle Donne, D., Genco, R., Maggio, G., Pistolesi, M., Marchetti, E., et al. (2015). Volcano seismicity and ground deformation unveil the gravity-driven magma discharge dynamics of a volcanic eruption. *Nature Communications*, *6*(1), 6998. https://doi.org/10.1038/ncomms7998

Ripepe, M., Delle Donne, D., Legrand, D., Valade, S., & Lacanna, G. (2021). Magma pressure discharge induces very long period seismicity. *Scientific Reports*, *11*. https://doi.org/10.1038/s41598-021-99513-4

Ripepe, M., Donne, D. D., Harris, A., Marchetti, E., & Ulivieri, G. (2008). *Dynamics of Strombolian activity* (Vol. 182, pp. 39–48). American Geophysical Union Geophysical Monograph Series.

Ripepe, M., Lacanna, G., Pistolesi, M., Silengo, M. C., Aiuppa, A., Laiolo, M., et al. (2021). Ground deformation reveals the scale-invariant conduit dynamics driving explosive basaltic eruptions. *Nature Communications*, *12*, 1683. https://doi.org/10.1038/s41467-021-21722-2

Ripepe, M., Marchetti, E., & Ulivieri, G. (2007). Infrasonic monitoring at Stromboli volcano during the 2003 effusive eruption: Insights on the explosive and degassing process of an open conduit system. *Journal of Geophysical Research*, *112*, B09207. https://doi.org/10.1029/2006JB004613

Ripepe, M., Pistolesi, M., Coppola, D., Delle Donne, D., Genco, R., Lacanna, G., et al. (2017). Forecasting effusive dynamics and decompression rates by magmastatic model at open-vent volcanoes. *Scientific Reports*, *7*, 3885. https://doi.org/10.1038/s41598-017-03833-3

Rosi, M., Pistolesi, M., Bertagnini, A., Landi, P., Pompilio, M., & Di Roberto, A. (2013). Stromboli volcano, Aeolian Islands (Italy): Present eruptive activity and hazards. *Geological Society London Memoirs*, *37*, 475–492. https://doi.org/10.1144/m37.14

Rowe, C. A., Aster, R. C., Kyle, P. R., Schlue, J. R., & Dibble, R. R. (1998). Broadband recording of Strombolian explosions and associated very-long-period seismic signals on Mount Erebus volcano, Ross Island, Antarctica. *Geophysical Research Letters*, *25*(13), 2297–2300. https://doi.org/10.1029/98GL01622

Seyfried, R., & Freundt, A. (2000). Experiments on conduit flow and eruption behavior of basaltic volcanic eruptions. *Journal of Geophysical Research*, *105*(B1023),23727–23740. https://doi.org/10.1029/2000JB900096

Stein, S., & Wysession, M. (2003). *An introduction to seismology, earthquakes, and earth structure*. Blackwell.

Suckale, J., Keller, T., Cashman, K., & Persson, P. O. (2016). Flow-to-fracture transition in a volcanic mush plug may govern normal eruptions at Stromboli. *Geophysical Research Letters*, *43*, 1–11. https://doi.org/10.1002/2016GL071501

Valade, S., Lacanna, G., Coppola, D., Laiolo, M., Pistolesi, M., Donne, D. D., et al. (2016). Tracking dynamics of magma migration in open-conduit systems. *The Bulletin of Volcanology*, *78*(11), 78. https://doi.org/10.1007/s00445-016-1072-x

Vergniolle, S. (1998). Modeling two-phase flow in a volcano. In *Proceedings of the Thirteenth Australasian fluid Mechanics Conference* (pp. 647–650). Monash University.

Vergniolle, S., & Brandeis, G. (1996). Strombolian explosions: 1. A large bubble breaking at the surface of a lava column as a source of sound. *Journal of Geophysical Research*, *101*(B9), 20433–20447. https://doi.org/10.1029/96jb01178

Vergniolle, S., & Jaupart, C. (1990). Dynamics of degassing at Kilauea volcano, Hawaii. *Journal of Geophysical Research*, *95*(B3), 2793–2809. https://doi.org/10.1029/JB095iB03p02793

Wilson, L. (1980). Relationships between pressure, volatile content and ejecta velocity in three types of volcanic explosion. *Journal of Volcanology and Geothermal Research*, *8*(2–4), 297–313. https://doi.org/10.1016/0377-0273(80)90110-9